

REPORT DOCUMENTATION PAGE

AFRL-SR-AR-TR-03-

Public reporting burden for this collection of information is estimated to average 1 hour per response, including the time for reviewing instructions, searching existing data sources, gathering the required information, reviewing and collecting the information. Send comments regarding this burden estimate or any other aspect of this collection of information, including suggestions for reducing the burden, to Washington Headquarters Services, Directorate for Information Operations and Reports, 1215 Jefferson Davis Highway, Suite 1204, Arlington, VA 22202-4302, and to the Office of Management and Budget, Paperwork Project, Washington, DC 20503.

0210

reviewing
information

1. AGENCY USE ONLY (Leave blank)		2. REPORT DATE	3. REPORT TYPE AND DATES COVERED 15 SEP 95 - 14 SEP 01	
4. TITLE AND SUBTITLE INTELLIGENT ELECTRONICS MANUFACTURING: MODELING AND CONTROL OF PLASMA PROCESSING			5. FUNDING NUMBERS F49620-95-1-0524	
6. AUTHOR(S) Pramod P. Khargonekar				
7. PERFORMING ORGANIZATION NAME(S) AND ADDRESS(ES) The University of Michigan Dept of Electrical Engineering and Computer Science Ann Arbor, MI 48109-2122			8. PERFORMING ORGANIZATION REPORT NUMBER	
9. SPONSORING/MONITORING AGENCY NAME(S) AND ADDRESS(ES) AFOSR/NM 4015 Wilson Blvd, Room 713 Arlington, VA 22203-1954			10. SPONSORING/MONITORING AGENCY REPORT NUMBER F49620-95-1-0524	
11. SUPPLEMENTARY NOTES <div style="text-align: right; font-size: 2em; font-weight: bold;">20030618 125</div>				
12a. DISTRIBUTION AVAILABILITY STATEMENT APPROVED FOR PUBLIC RELEASE, DISTRIBUTION UNLIMITED			12b. DISTRIBUTION CODE	
13. ABSTRACT (Maximum 200 words) The MURI Center on Modeling and Control of Plasma Processing at the University of Michigan started in September, 1995, and concluded technical work at the end of August 2001. As the name indicates, the major research goals of the center are in the areas of modeling and control of plasma deposition and etching processing. These plasma processes are used extensively in the manufacture of integrated circuits as well as active matrix liquid crystal displays. These applications areas motivate our selection of research problems in modeling and control. Significant accomplishments were made in all of these areas (as will be discussed in the body of the report). Particular program highlights include: (1) An optical technique was developed to monitor in situ and in real time the critical dimensions and wall-shapes of evolving features in reactive ion etchers. An advanced signal processing scheme was devised to use this technique to perform the first fully-automated etch-to-target-dimension etches. One-nanometer-level (or better) accuracy was demonstrated enabling possibilities for extremely high accuracy semiconductor fabrication control. (2) The state-of-the-art of 1st principles plasma equipment modeling was advanced so that the entire system of the sensors, plasma process equipment, and control systems could be modeled numerically. (3) Novel RF Sensing to non-invasively measure the electrical state of plasma systems was developed and applications to detecting common faults were demonstrated. (4) Improved statistical methods for detecting and identifying the causes of spatially clustered defects in semiconductor manufacturing. (5) Development of a novel ion-beam modification process for the deposition of Al films which are more resistant to grain-growth.				
14. SUBJECT TERMS			15. NUMBER OF PAGES 64	
			16. PRICE CODE	
17. SECURITY CLASSIFICATION OF REPORT	18. SECURITY CLASSIFICATION OF THIS PAGE	19. SECURITY CLASSIFICATION OF ABSTRACT	20. LIMITATION OF ABSTRACT	

Final Report

AFOSR/DARPA MURI CENTER

INTELLIGENT ELECTRONICS MANUFACTURING:
MODELING AND CONTROL OF PLASMA PROCESSING

AFOSR GRANT NO. F49620-95-1-0524

May 13, 2003

Principal Investigator:
Pramod P. Khargonekar

Final Report by:
Fred Lewis Terry, Jr. (co-PI)

Dept. of Electrical Engineering and Computer Science
The University of Michigan
Ann Arbor, MI 48109-2122
Tel (734) 763-9764
Fax (734) 763-9324
Email fredty@umich.edu

Table of Contents

1	CENTER OBJECTIVES AND THE STATUS OF THE EFFORT	3
2	PLASMA PROCESS FIRST PRINCIPLES MODELING	5
3	SENSORS: MODELING, SIGNAL PROCESSING, AND CONTROL	18
31.	RF Sensing	18
32.	Wafer State Sensing – Spectroscopic Ellipsometry and Spectral Reflectometry.....	29
4	CONTROL	38
41.	Real-Time State Estimation for Patterned Wafers.....	38
42.	Design of Experiments	50
5	PROCESS AND MATERIALS RESEARCH	54
6	FACULTY, STAFF, AND STUDENTS SUPPORTED.....	55
7	PUBLICATIONS	56
8	INDUSTRIAL INTERACTIONS AND TRANSFER	62
9	HONORS AND AWARDS	64

1 Center Objectives and the Status of the Effort

The MURI Center on Modeling and Control of Plasma Processing at the University of Michigan started in September, 1995, and concluded technical work at the end of August, 2001. As the name indicates, the major research goals of the center are in the areas of modeling and control of plasma deposition and etching processes. These plasma processes are used extensively in the manufacture of integrated circuits as well as active matrix liquid crystal displays. These applications areas motivate our selection of research problems in modeling and control.

The major goal of this MURI Center was to develop basic science and technology to enable significant improvements in the robustness and performance of plasma etching and deposition used in microelectronics manufacturing. The research strategy was to use a synergistic combination of modeling, sensors, and control. We were also focused on the ultimate manufacturing applications, which will impact cost and quality of the microelectronics products. In turn this will be of benefit to the Department of Defense.

Over the contract period, we focused on the following main topics:

1. Modeling - first principles plasma modeling and statistical process modeling
2. Plasma sensors - RF sensing, optical emission sensing, CF_2 sensing
3. Wafer sensors: Modeling, Signal Processing, and Control
4. Real-time control using both process and wafer sensors
5. Process and materials research

Significant accomplishments were made in all of these areas (as will be discussed in the body of this report). Particular program highlights include:

1. An optical technique was developed to monitor *in situ* and in real-time the critical dimensions and wall-shapes of evolving features in reactive ion etchers. An advanced signal processing scheme was devised to use this technique to perform the first fully-automated etch-to-target-dimension etches. One-nanometer-level (or better) accuracy was demonstrated enabling possibilities for extremely high accuracy semiconductor fabrication control.
2. The state-of-the-art of 1st-principles plasma equipment modeling was advanced so that the entire system of the sensors, plasma process equipment, and control systems could be modeled numerically.
3. Novel RF Sensing to non-invasively measure the electrical state of plasma systems was developed and applications to detecting common faults were demonstrated.
4. Improved statistical methods for detecting and identifying the causes of spatially clustered defects in semiconductor manufacturing
5. Development of a novel ion-beam modification process for the deposition of Al films which are more resistant to grain-growth.
6. Development of improved plasma deposition processes for the manufacture of high performance AMLCDs.

The most striking of these results is item 1, the development of both physical sensing methods to accurately extract deep sub-micron topographic information *in situ* and in

real-time, and the control/signal processing methodology to make use of this information for very high accuracy etch process control. This set of results has attracted a great deal of attention in both scientific and industrial communities. Frankly, this level of success was well beyond what we had anticipated at the beginning of this project. It was the directly the result of the ability offered by this MURI to combine the efforts of researchers in multiple separate disciplines to focus on a very significant problem.

Some aspects of the research successes of this program, including the in situ topography measurement and control were pushed further under a NIST-ATP program, "Intelligent Control of the Semiconductor Patterning Process," (cooperative agreement No: 70NANB8H4067). Under this ATP effort several result of the research of this MURI program were extended and pushed closer to industrial application:

- The Broadband RF sensor (section 3.1) was extended to full real-time feedback control of plasma density and very significant stabilization of Cl_2 etching of Si was achieved.
- The real-time optical topography methods were further developed and demonstrated to industry. While the industry is not yet ready for the in situ, real-time application, these successful demonstration have helped speed the application of the still useful but more conservative in-line, wafer-to-wafer control approach.
- Industrial applications of combined feed-back/feed-forward control methods were made involving University of Michigan developed algorithms being implemented at Lam Research Corp. using KLA-Tencor in-line metrology tools on Motorola wafers.

In summary, we believe that this MURI program achieved major technical successes that were the direct result of synergistic activities among researchers who otherwise would not have had the resources and freedom to work together on these problems. Some of these successes have already been internationally recognized, and industrial applications are already being made. The technology transfer was facilitated by the ATP program mentioned above, but there was also technology transfer directly through our published papers. For instance, we learned at a major symposium on process control that an engineer at Micron Technologies had read our papers on extended Kalman filtering for thin film thickness monitoring and had directly applied them to his production development problems. While it difficult or impossible to document this impression, we believe that the successes of this program (and those of the other MURI efforts in this series) significantly helped with the semiconductor industry's move toward real use of advanced process control.

2 Plasma Process First Principles Modeling

The University of Illinois (UI) research tasks were to develop plasma equipment models as vehicles to both test control strategies for plasma etching and deposition tools, and to generate system performances and responses for parameters which might otherwise be difficult to experimentally provide. The motivation for this work is that if one can develop a sufficiently comprehensive computational representation of the plasma equipment, realistic sensor inputs can be provided for a controller; and the control directives can be implemented on a "virtual basis". In doing so one can speed the development time for new control methodologies and do so with more physical understanding of the process.

The foundation for our modeling activities is the Hybrid Plasma Equipment Model (HPEM). The HPEM is a comprehensive plasma equipment simulator which is able to address a wide variety of tools, including reactive ion etching (RIE) and inductively coupled plasma (ICP) sources. In a subset of our MURI research tasks, we are continuing technical development of the HPEM to improve its capabilities. During the MURI we have developed an interface to the HPEM which provides virtual sensor inputs and actuator directives to the HPEM from a controller module (CM). We call this framework the Virtual Plasma Equipment Model (VPEM). (See Figure 1) Conceptually, we treat the VPEM exactly as one would treat an experimental plasma tool equipped with sensors and actuators. We specify operating conditions, sensor inputs and control points, and a desired mode of operation. We then perturb the system. The CM takes the sensor inputs, implements a control strategy, and specifies actuator directives which bring the plasma tool back onto desired operating specifications. Using the VPEM, a number of scenarios have been investigated in which response surface and PID based controllers were used to compensate for external disturbances, nullify the effect of long term drifts and improve uniformity.

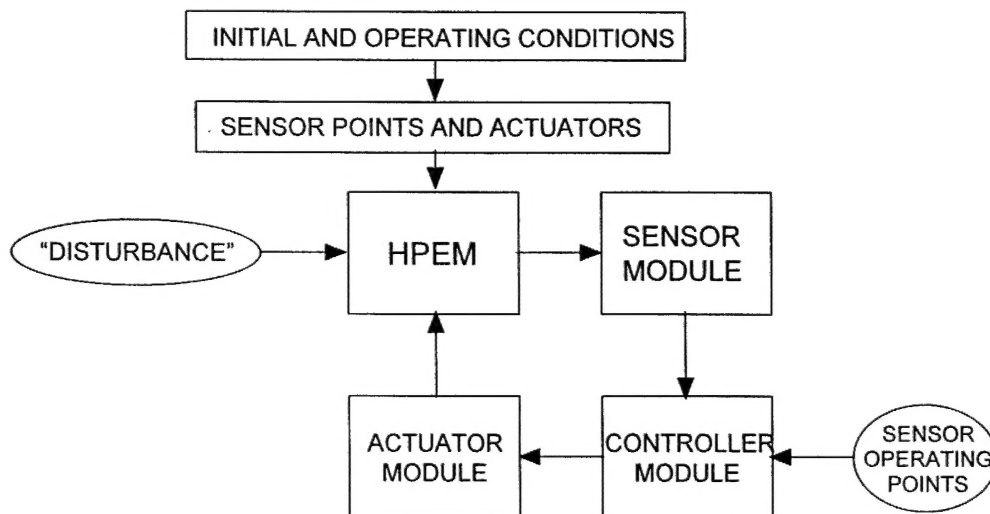


Figure 1 Schematic of the Virtual Plasma Equipment Model (VPEM).

As an example of these capabilities, we demonstrate the use of the VPEM to investigate pulsed plasma processing and, in particular, controlling transients during, for example, recipe changes. We highlight one study in which we investigated the appropriateness of using actinometry sensors during a transient where the wall sticking coefficient of Cl atoms changes due to, for example, a recipe change. The densities of Ar, Cl and Cl₂ in an inductively coupled plasma during a transient where the wall reassociation coefficient of Cl atoms increases by a factor of 4 are shown in Fig. 2. The density of Cl decreases, while those for Ar and Cl₂ increase. The Ar density increases because the total flowrate has decreased in order to keep the pressure and mass flux constant while the Ar fractional flow rate remains constant.

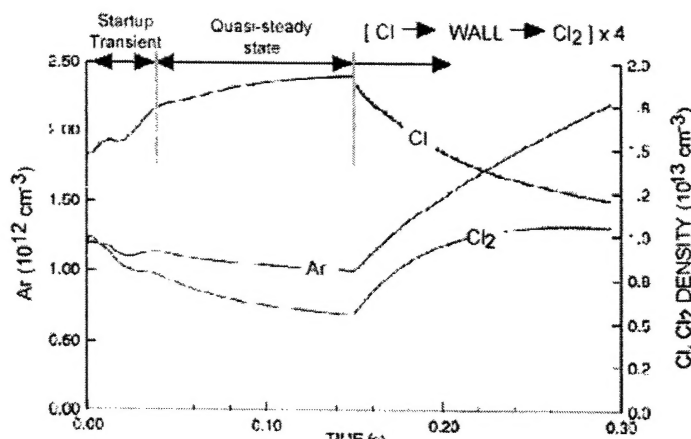


Figure 2 Densities in an ICP reactor during a transient during which the wall recombination rate of Cl atoms increases.

Densities in an ICP reactor during a transient during which the wall recombination rate of Cl atoms increases.

An actinometry sensor was used to maintain the density of Cl atoms constant using a PID controller. The actinometry signal is the ratio of optical emission Cl^*/Ar^* . The actinometry signal closely follows the Cl density prior to the transient, as shown in Figure 3. After the transient the actinometry signal and Cl density (in the absence of control) diverge. This occurs because, while keeping the pressure and mass flux constant, the mole fraction of Ar in the system increases. As a result, the denominator in the actinometry sensor increases, making the signal decrease relative to the Cl density.

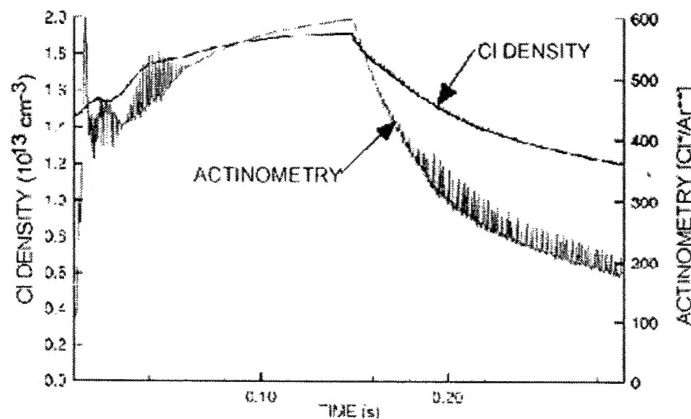


Figure 3 Actinometry signal and actual Cl density before and during the transient.

When one then tries to control this transient using a PID controller (which equates Cl^* signal to power deposition), the response is to recommend an increase in power. The increase in power produces an increase in gas temperature and a commensurate decrease in gas densities which further "motivates" an increase in power. (See Figure 4) The end result is that the system goes unstable.

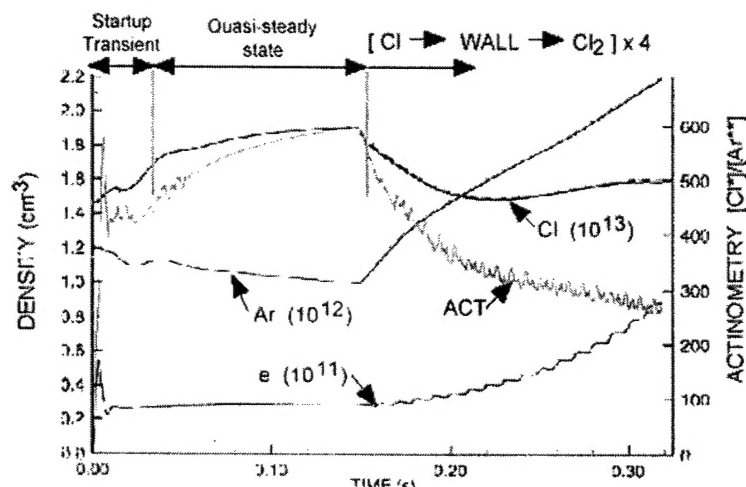


Figure 4 Actinometry signal and species densities before and during the transient when using a PID controller.

It is important, then, to choose sensors and actuators which are well correlated in well behaved manner over large dynamics ranges. The choice of such sensors is often not immediately obvious. Through the use of the VPME, such sensors can be selected. For example, we revisit the control problem in a chlorine inductively coupled plasma where the wall sticking coefficient for $\text{Cl} \rightarrow \text{Cl}_2$ on the walls impulsively increases. This

change in sticking coefficient not only changes the magnitude of fluxes to the substrate but also their uniformity. For example, the densities of Cl and Cl₂ in an inductively coupled plasma with the operating conditions Ar/Cl₂ = 50/50, 20 mTorr, 500 W, 200 sccm are shown in Figure 5. The corresponding changes in ion flux and uniformity are shown in Figure 6.

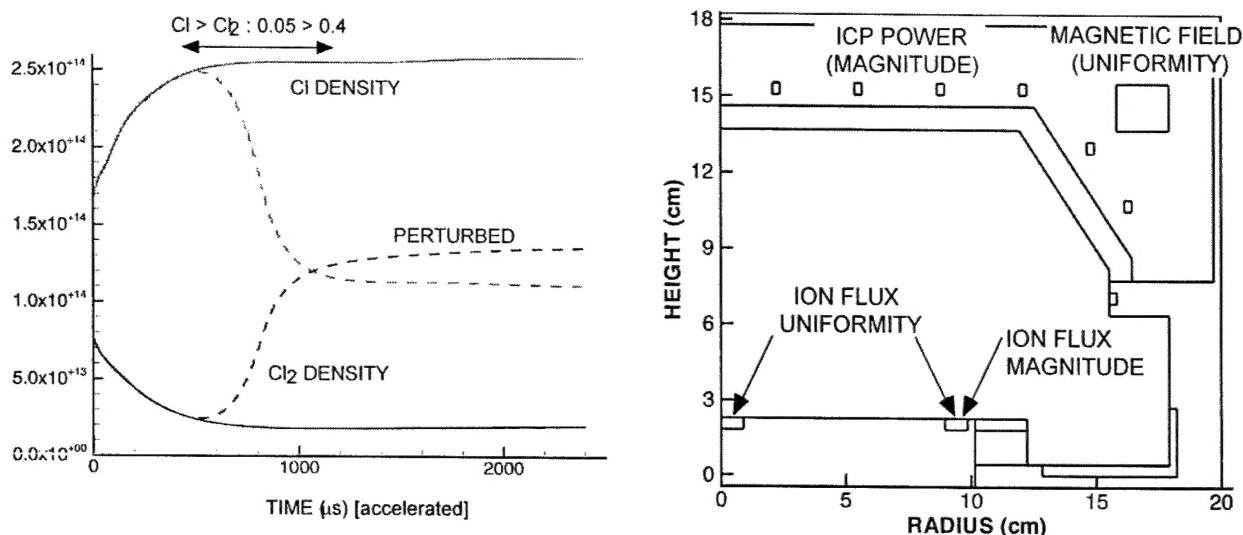


Figure 5 Densities of Cl and Cl₂ in an ICP reactor following a change in sticking coefficient.

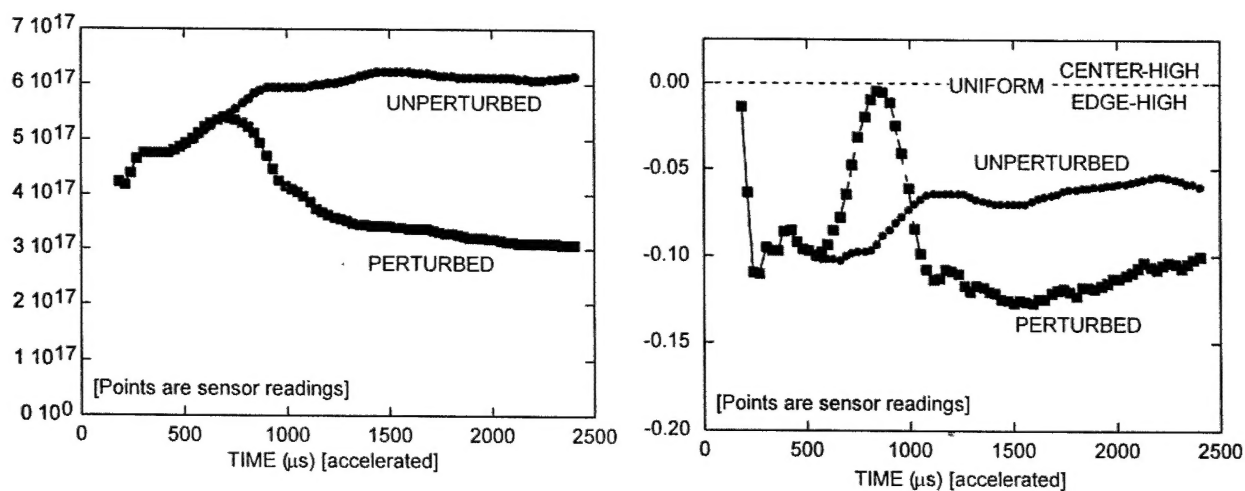


Figure 6 Ion flux and uniformity of the ion flux resulting from a change in wall sticking coefficient.

Through parameterization of the VPDM, we found that ion flux was well controlled by ICP power and ion flux uniformity could be controlled by use of a static magnetic field. The control of ion flux by power deposition is straightforward. The control of ion flux uniformity by use of a magnetic field results from a change in the spatial distribution

of power deposition. In short, the plasma tensor conductivity in the presence of a static magnetic field “pushes” power deposition around by generating additional components of the inductively coupled electric field. These trends are demonstrated in Figure 7 where power deposition with and without a 5 G magnetic field is shown.

Using 2 PID controllers, correlating power deposition (actuator) with ion flux (sensor); and magnetic field (actuator) with ion flux uniformity (sensor), a control strategy was developed which maintained the magnitude and uniformity of the ion flux through the transient. These results are shown in Figure 8.

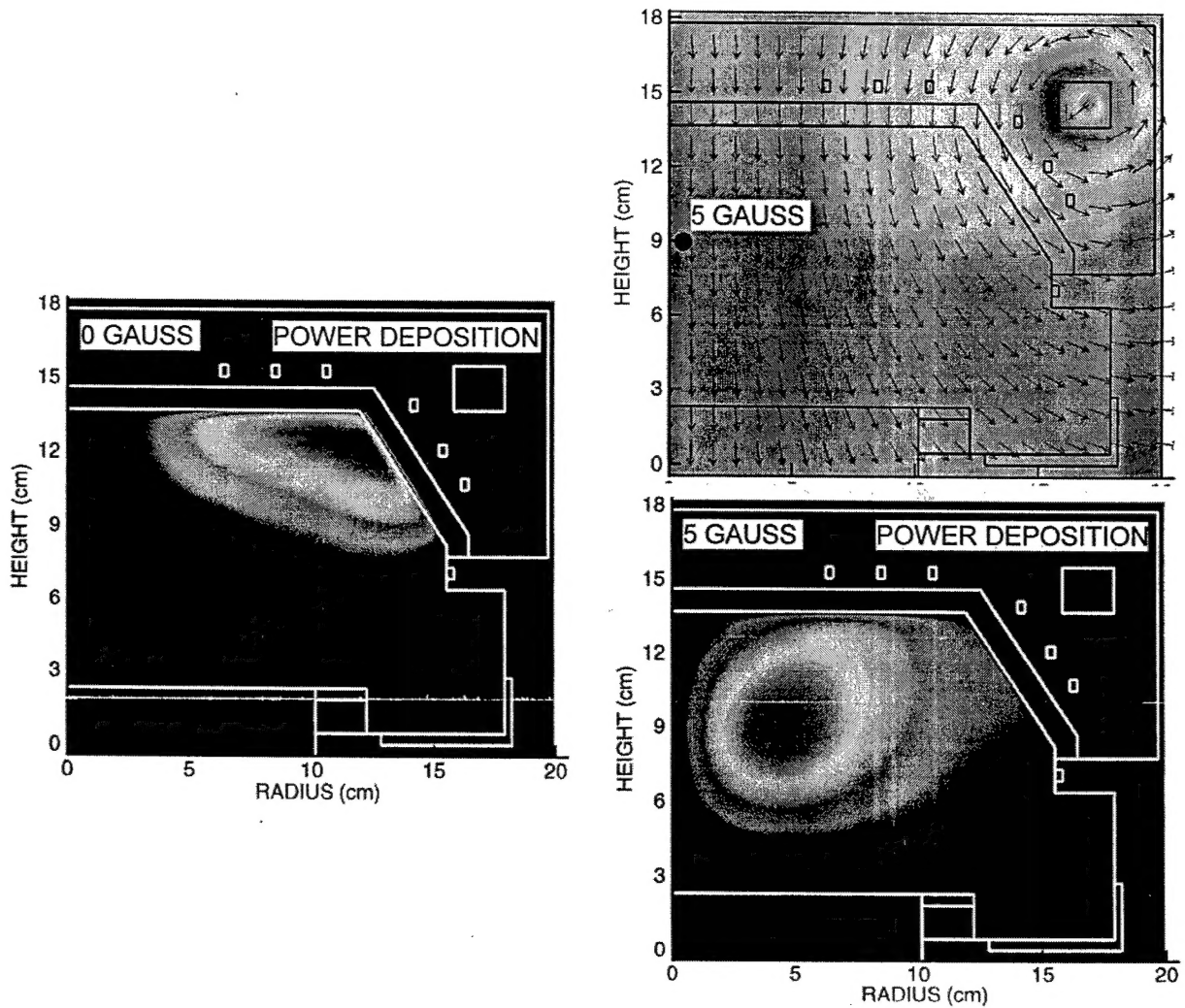


Figure 7 Power deposition with no magnetic field and a magnetic field of 5 G. The magnetic field vectors are shown at right.

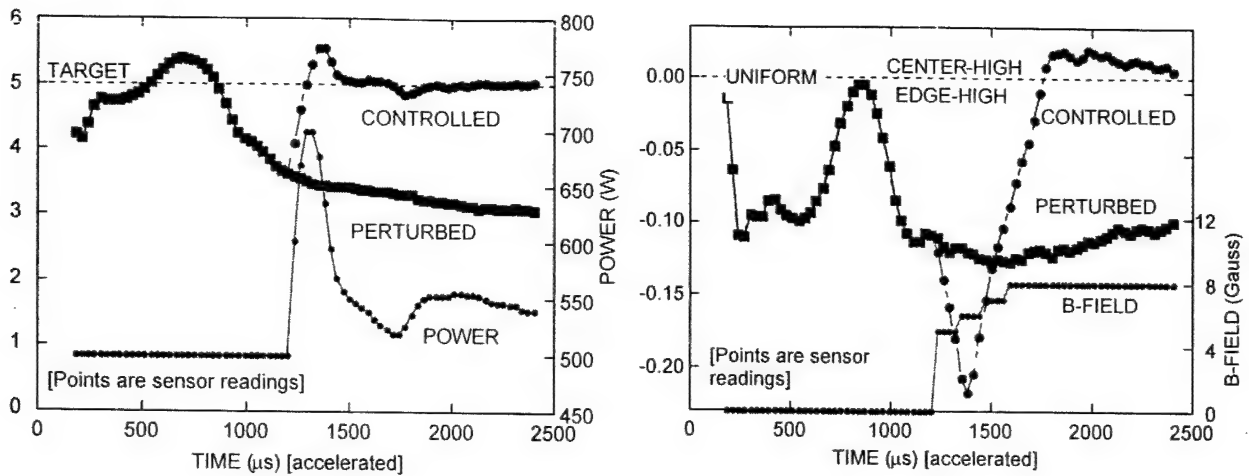


Figure 8 Ion flux and uniformity of the ion flux resulting from a change in wall sticking coefficient using 2 PID controllers having ICP power and magnetic fields as actuators.

Another control strategy we investigated was how to address conditions which may greatly deviate from expected or "base case" operation. In the discussion that follows, the reactor shown schematically in Figure 9 will be used. This is an inductively-coupled-plasma (ICP) reactor excited by a 3 coils. Gas is injected into the reactor through a showerhead nozzle and exhausted at the bottom. Sensors include a Langmuir probe to measure electron density, a surface electrical probe to measure ion current, a mass spectrometer and observations of optical emission from three locations above the wafer. The optical emission measurements will be used to gauge uniformity of etching on the wafer. The actuators include gas pressure, ICP power deposition and the relative amount of current flowing through the 3 ICP coils which can be used to affect plasma uniformity.

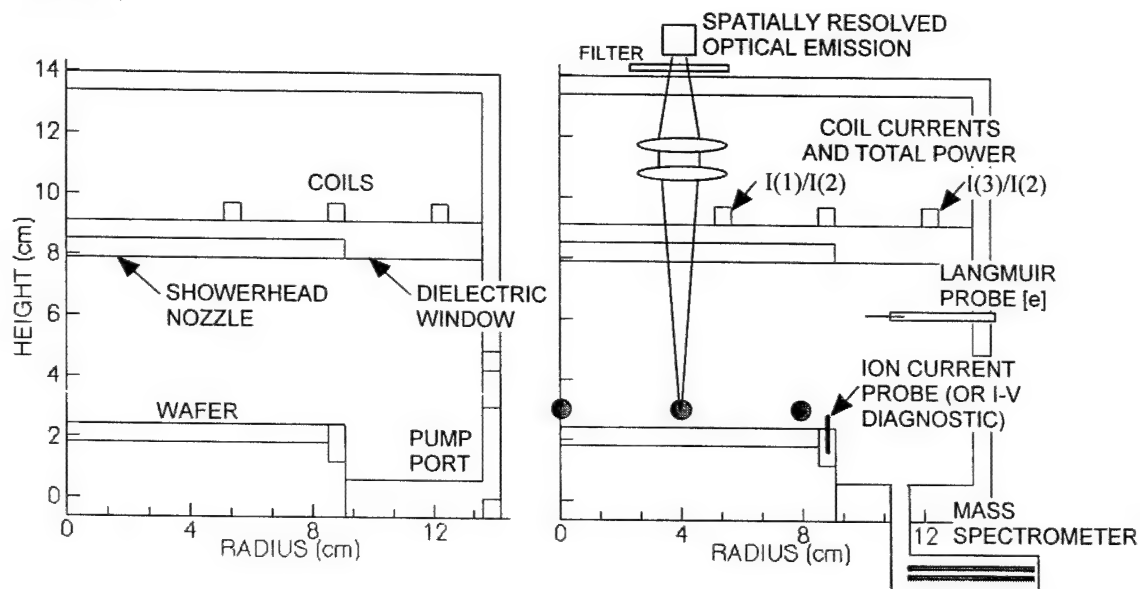


Figure 9 Schematic of the ICP reactor used to develop strategies for stabilizing reactor performance through transients.

The first example we will discuss is for an ICP reactor operating in pure argon when a "puff" of nitrogen gas is released into chamber. This simulates a transient failure in a mass flow controller. The Ar^+ and electron densities during this transient are shown in Figure 10. The conditions are 10 mTorr with 250 sccm of gas flow. When 25 sccm of nitrogen are "puffed" into the reactor, the total electron density (now balanced by Ar^+ and N_2^+) decreases because N_2 dissipates more power in non-ionizing collisions than does argon. As the N_2 flows into a larger volume of the reactor, the plasma density continues to decrease. After the mass-flow-controller is corrected and the N_2 stops flowing, there is a clearing time for the N_2 to exhaust from the reactor, during which the plasma density recovers to its original value.

A 2 x 2 response surface based controller was formulated using power and pressure as the actuators, and electron density and ion current to the substrate as sensors. The results of the control exercise are shown in Figure 11. The electron density is only mildly stabilized because the controller has insufficient information on "future" conditions. Sensor readings are made when the plasma is responding to a particular mole fraction or spatial distribution of N_2 . The recommended actuator settings are then implemented based on these sensor signals. When the N_2 density is increasing, conditions continually worsen, and so the recommended changes in actuator settings soon become too small to restore the sensors to their target values. The sensor readings initially move towards their target values, but then begin to deviate. When the N_2 density is decreasing, conditions continually improve after the sensor readings and actuator changes, and a similar situation results, though the sign of the recommended change in actuator settings reverses. These are conditions which are not well addressed by, for example, PID controllers.

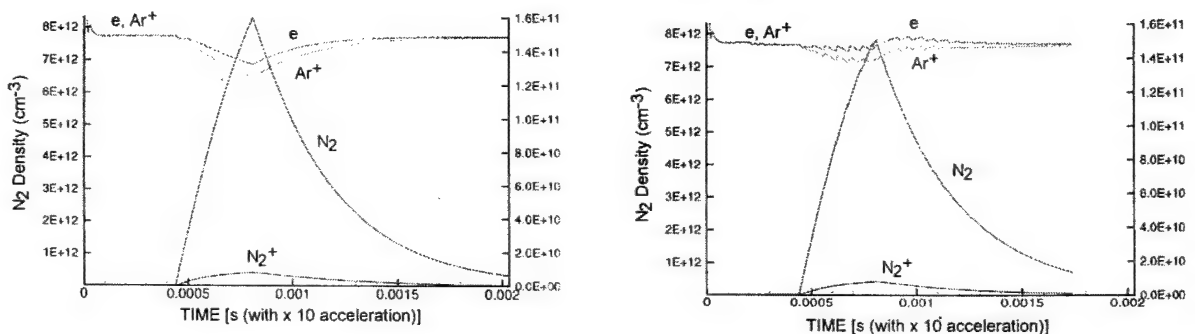


Figure 10 (left) Electron and ion densities during a transient where an errant mass flow controller "puffs" N_2 into an ICP reactor.

Figure 11 (right) Electron and ion densities when control is applied to stabilize the electron density during a transient where N_2 is "puffed" into an ICP reactor.

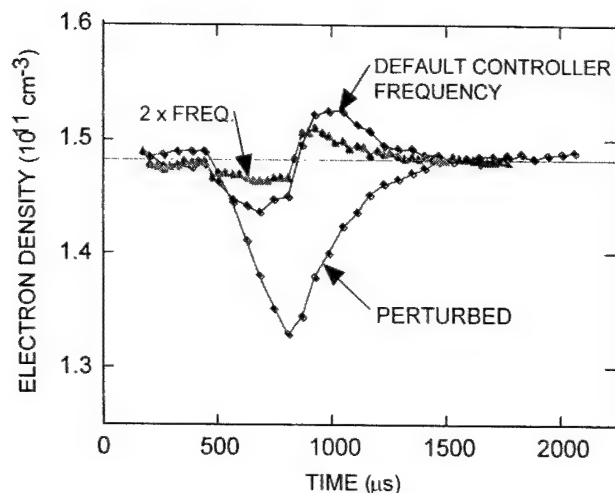


Figure 12 Electron density in the ICP reactor with a N_2 gas leak at times of sensor readings for the uncontrolled case, control at the default frequency and at twice the default frequency.

There are at least 3-strategies to correct for these changes in operating conditions: 1) Increase the frequency of the controller so that lack of future information is not as critical. 2) Build in knowledge of the characteristics of the perturbed system into the controller. 3) Dynamically adjust gain to compensate for under- (or over-) predicting changes in actuator settings. Option 2 is difficult to employ if the goal is to control against unpredictable transients. Option 1 has physical limitations in that there is a practical upper limit to the controller frequency. For example, the electron densities in the ICP during the N_2 puff at the time of sensor readings are shown in Figure 12 for the perturbed (uncontrolled) conditions, with control at the default frequency and with control twice the default frequency. The poor knowledge of the future resulting in under predicting changes in actuator settings is somewhat compensated for by the increase in controller frequency.

There is, however, a common procedure where "knowledge of the future" can be used to control against transients. This procedure is change in recipe where, for example, the power or gas mixture are changed as one transitions between the "main etch" and the "overetch". We investigated the recipe change of switching from an $Ar/Cl_2=90/10$ gas mixture to an $Ar/Cl_2=99/1$ mixture. The densities of Ar, Cl and Cl_2 during the transient (250 sccm, 10 mTorr) are shown in Figure 13. Uniformity will be controlled using optical emission from Cl^* from three locations above the wafer as shown in Figure 14. The actuators will be the relative amount of current flowing through the inner and outer coils. The problem is that as the Cl_2 mole fraction changes during the transient, the response surfaces which are used to determine actuator adjustments also change. Knowing ahead of time that the transient involves a change in Cl_2 mole fraction (this is

your "knowledge of the future"), one can use an additional sensor, in this case a mass spectrometer, to measure the Cl_2 mole fraction. This additional data is then used to interpolate between response surfaces which were prepared for different Cl_2 mole fractions in steady state experiments. This is called using additional "planes" of response surfaces. Using more planes should yield better results since the coefficients used for any given Cl_2 mole fraction are more representative of the instantaneous conditions.

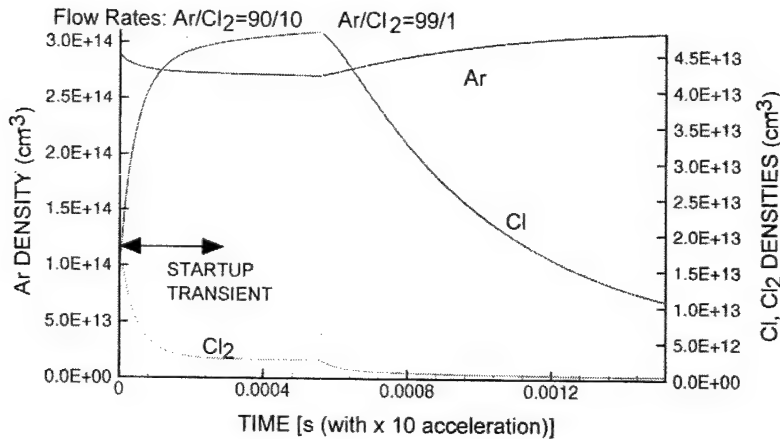


Figure 13 Densities of Ar, Cl and Cl_2 during a recipe change (250 sccm, 10 mTorr).

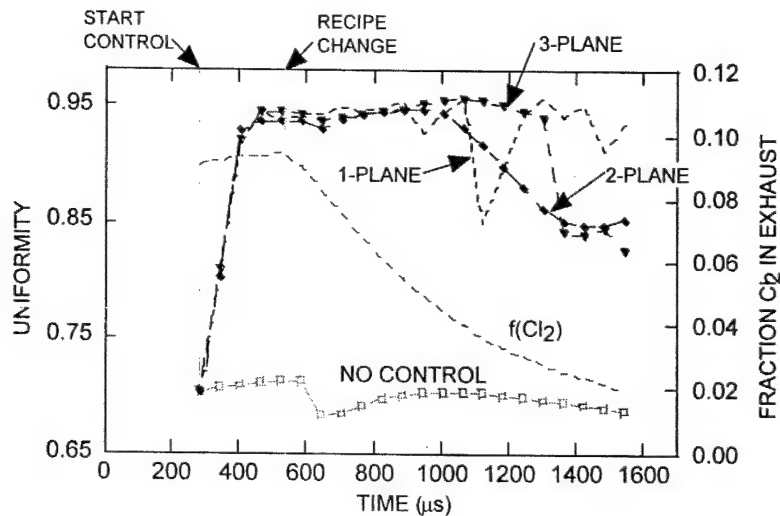


Figure 14 Uniformity of optical emission from Cl^* during a recipe change using 1, 2 and 3 planes of control (250 sccm, 10 mTorr).

An example of stabilizing uniformity through a recipe change is shown in Figure 14. The uniformity parameter α without control [α ranges from (0,1) from poor to perfect

uniformity] is 0.68-0.71. With control α is improved to 0.95. The length of time which α can be held at a high value increases as the number of planes of control increase.

A major portion of our efforts were devoted to the development of more robust and comprehensive plasma models, as embodied in the HPEM/VPEM, to address a wider variety and complexity of plasma tools. In work jointly funded by the National Science Foundation, Semiconductor Research corporation, Applied Materials and LAM Research Corporation, significant new capabilities were developed, as discussed in the attached publications. One such development is described here.

Major modifications were made to the HPEM to enable simulation of long-term transients and pulsed plasmas. The HPEM was converted to a moderately parallel code wherein each of the major modules are executed on different processors. This enables plasma properties being updated in, for example, the fluid kinetics module to be made immediately available, through shared memory, to the electron Monte Carlo Simulation. This methodology is schematically shown in Figure 15. These algorithms were implement using OPEN-MP protocols on a 4-processor Sun-Microsystems server. This has resulted, to our knowledge, in the first 2-dimensional fully transient plasma equipment model.

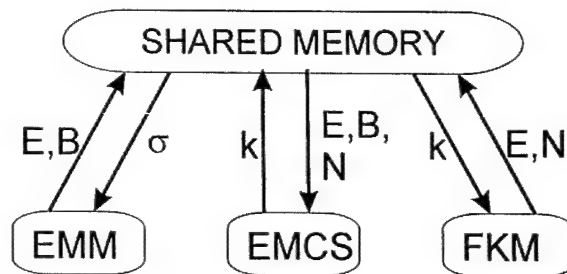


Figure 15 Schematic of the parallel HPEM which exchanges plasma properties through shared memory.

Examples of the results from the parallel HPEM are shown in Figs. 16-18. The electron density and plasma potential during pulsed operation of the ICP GEC Reference Cell are shown in Figure 16. The operating conditions are Ar/Cl₂=80/20, 20 mTorr, 300 W with a 30% duty cycle at 10 kHz. Due to enhanced attachment in the afterglow when power is turned off producing a fall in the electron temperature, the electron density decreases to a few percent of its peak. The plasma potential then falls to a few tenths of a volt. The plasma potential first drops rapidly due to electron cooling, then less rapidly due to electron attachment. As a consequence of the drop in plasma potential negative ions, which would normally be trapped by the positive plasma potential, are able to escape the plasma and reach the substrate. This negative ion flux is important to neutralizing plasma induced damage of microelectronic components.

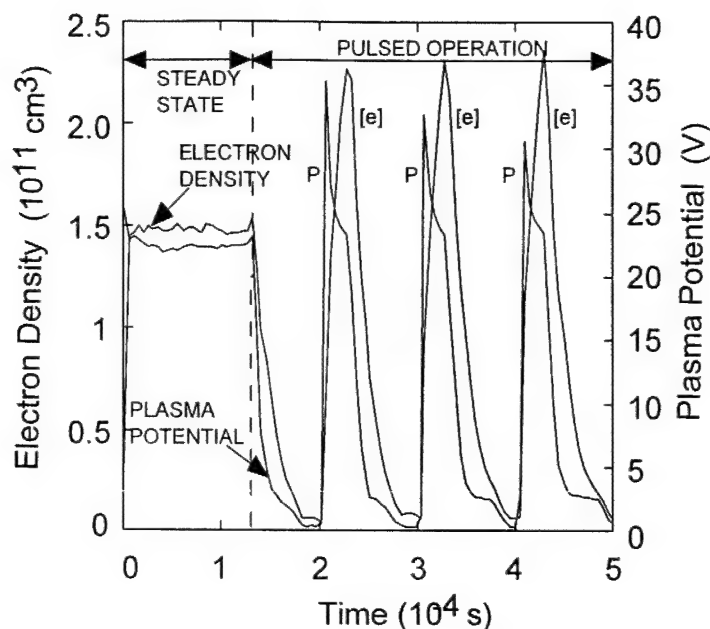


Figure 16 Electron density and plasma potential during pulsed operation of an ICP reactor. The pulse repetition rate is 10 kHz and the duty cycle is 30%.

For example, the plasma potential and negative ion flux vectors are shown in Figure 17 for conditions similar to those discussed above. The charged particle fluxes to the substrate are shown in Figure 18. During the period that power is on, the negative ion flux vectors point into the plasma where negative ions are consumed by ion-ion neutralization. When the power is turned off at 50 μ s, the plasma potential collapses. The negative ion flux vectors then turn, in a wave like manner, to pointing towards surfaces, indicating that the negative ions can escape from the plasma. As the chlorine fraction increases, the rate of collapse of the electron density and plasma potential increases, thereby enabling negative ions to more rapidly escape from the plasma. Negative ion are then incident on the substrate for a longer period of time.

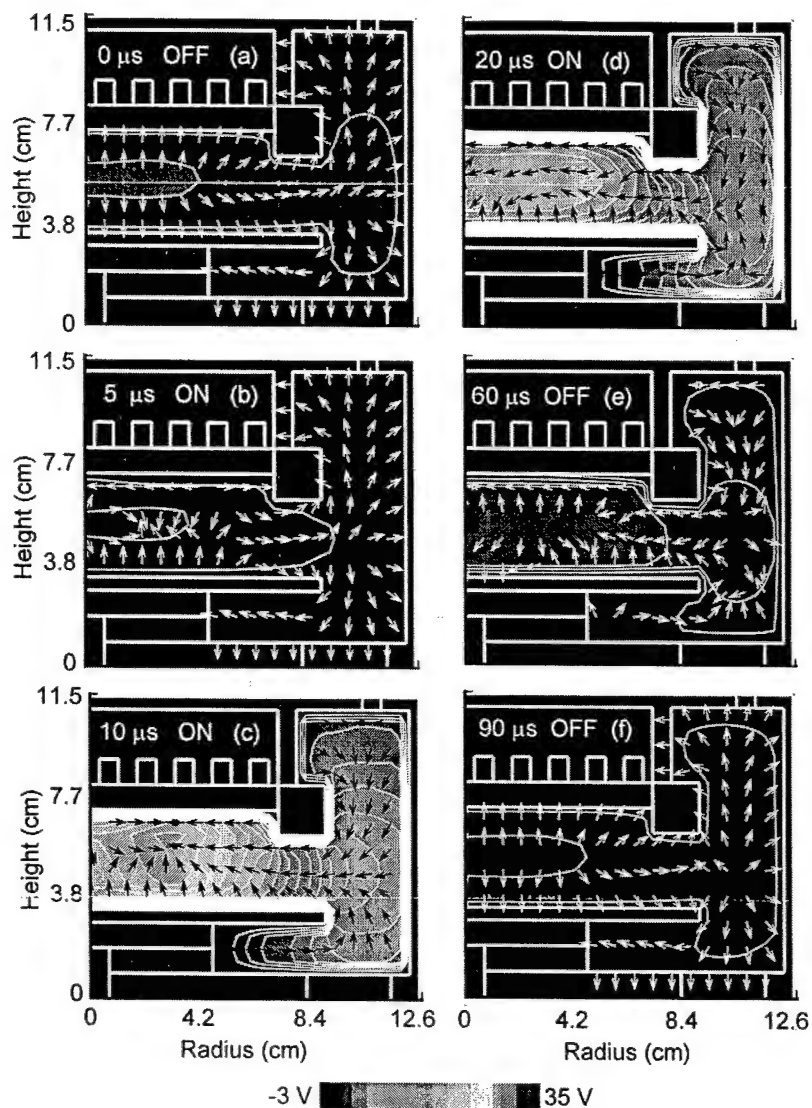


Figure 17 Cl⁻ negative ion flux and plasma potential in Ar/Cl₂ plasmas at different times for a power of 300 W, PRF of 10 kHz and duty cycle of 50%. (Cl⁻ flux vectors are all of the same length and not scaled with respect to magnitude). Results are shown for a) 0 μs, b) 5 μs, c) 10 μs and d) 20 μs during the power-on period and e) 60 μs and f) 90 μs during the afterglow. Negative ions are extracted only after 70 μs into the afterglow.

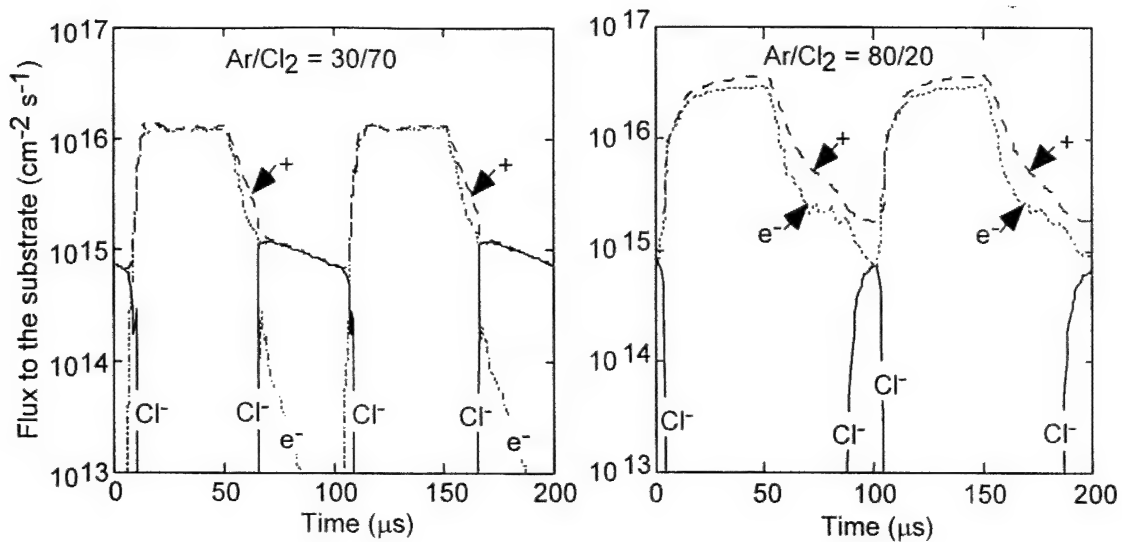


Figure 18 The temporal dynamics of positive ion, electron and Cl^- flux to the substrate as a function of Cl_2 fraction for $\text{Ar}/\text{Cl}_2 = 30/70$ and $\text{Ar}/\text{Cl}_2 = 80/20$. As the Cl_2 fraction increases, negative ions can be extracted for longer period in the afterglow.

3 Sensors: Modeling, Signal Processing, and Control

Our general strategy for plasma process control involved the use of:

- *process sensors* for high-speed feedback control, and;
- *substrate (wafer) sensors* for high accuracy endpoint detection and for process state to wafer state model construction and verification.

Our process state sensor efforts were concentrated on two areas: (1) measurement of the electrical state of the plasma through advanced RF measurements; and, (2) the measurement of polymer precursors (CF_2) in CF_4 plasmas. The major results of the latter work on CF_2 sensing has been desired in prior technical reports in this program and will not be repeated here. The RF measurement work proved to be more successful in the process control work in this program and will be summarized in section 3.1.

Our wafer state measurements continue to be focused on reflected light measurements (reflectometry and ellipsometry). Our major emphasis in this area is to try to extend our previously reported successes in automate endpoint detection using Extend Kalman Filtering to patterned wafers.

3.1 RF Sensing

Feedback control and diagnostics, whether implemented in a run-to-run or real-time fashion, require sensed information about the process and/or its environment. The overarching goal of this project is to obtain real-time process information through non-intrusive means. The term *RF sensing* typically refers to the action of measuring the 13.56 MHz RF signal used to strike a plasma in a plasma etch or deposition tool, and extracting information about deposited power, impedance, and strength of harmonics induced by the nonlinearities in the plasma and etch chamber. The first part of our work focused on quantifying in a rigorous manner the well-posedness of this measurement and its potential for providing reliable process information. We concluded that the RF measurement techniques used at the time in industry and academia, and marketed by several suppliers, were fundamentally flawed and could not be ameliorated in any practical manner. Our research in the MURI Program has done much to explain limitations of previous work in this area. We therefore embarked on the development of a novel sensor based on plasma impedance spectroscopy. This second phase of our research resulted in the design of a minimally-intrusive, Broadband RF sensor that has a one hundred- (100) to one thousand- (1,000) fold increase in sensitivity to conditions in the plasma. This sensor operates in the 300 MHz to 2 GHz range and responds to changes in deposited power, chemical concentration, pressure, and even certain aspects of the wafer's state. In the third phase of our research, we implemented this sensor on our Lam etch tool and developed signal processing techniques to extract information from the Broadband RF sensor. We demonstrated the combination of the sensor and algorithms on Si etch rate extraction and actuator fault detection and isolation. This section details our accomplishments in RF sensing over the period of this contract.

3.1.1 RF Sensing at 13.56 MHz

Plasma processing specialists in industry and academia had recognized that a substantial amount of information about the plasma state should be contained in the RF signal (13.56 MHz) and its harmonics. On the surface, making current and voltage measurements should be straightforward, and the real work should lie in developing the mathematical models between measurements and key plasma quantities (absorbed power, electron concentration and temperature, ion concentration, etc.). Unfortunately, this is not the case. Work reported in this area from Stanford, Berkeley, MIT, Texas-Austin and NIST, as well both US and Japanese chip manufacturers, has revealed that the RF sensing problem itself at the 13.56 drive frequency is non-trivial. In particular, one of our original industrial partners, Optical Imaging Systems, tried off-the-shelf RF technology, and it failed.

Our work has investigated the fundamental issues that determine the limits on the accuracy with which RF signals can be measured in a plasma environment. We have investigated this with respect to properties of the reactor (high density, low density, pressure range and type of processing gas), the choice of RF probe technology (coupler based or current voltage based), and with respect to the receiver technology (vector network analyzer, power meter, vector voltmeter or digital oscilloscope). We have shown that the single most important factor affecting the success of RF monitoring at these frequencies is the voltage standing wave ratio (VSWR) of the RF power system. The VSWR is determined by the reactor's density, pressure range and process gases. A typical low-density (single source, capacitively coupled) plasma system at 20 mTorr with fluorocarbon chemistry, as is commonly used in the display industry, will have a VSWR of around 50. Under these conditions, we have shown that an inaccuracy in the raw voltage and current measurement at the sensor is magnified one hundred fold in the computation of deposited power. The second most important factor in determining accuracy is the quality of the model that relates sensor measurements to the measured electrical state. Our work has revealed that a directional coupler in tandem with a high quality receiver is inherently more linear than a current voltage probe with an oscilloscope. The relationship between the true electrical state as established by a network analyzer and the measurement of the directional coupler can be modeled very accurately by a two port electrical network. Other choices of sensor-receiver combinations turn out to be quite nonlinear, and require an inordinate number of data points for calibration (i.e. accurate model building).

	Raw Data	Model Based Correction
Laboratory Quality Measurements	4.28%	0.98%
Realistic Probe Receiver Combination	21.30%	12.8%
Common Practice	122.40%	145%

Table 1 Comparison of relative errors in computed power at a VSWR of 50. The realistic probe receiver combination consists of a pair of power meters and a directional coupler. A dual channel power meter should further reduce the error by half over a pair of power meters.

We also developed two-port models for the reactor chamber and its power connections, allowing us to de-embed it from the electrical measurements, and hence accurately

estimate the power absorbed by the plasma itself (instead of the plasma and chamber), as well as the plasma impedance. This in turn has led to direct feedback control of the plasma via electrical measurements and the on-line estimation of quantities such as sheath thickness and electron concentration on our Applied Materials 8300 reactor.

Armed with our knowledge of the limitations of RF sensing at 13.56 MHz, we investigated the use of the sensor for closed-loop control of the power deposited in the plasma. The fundamental idea was to control the power delivered to the plasma independently of losses in the delivery mechanism. The realization of the control system requires highly accurate sensing of the power delivered to the plasma chamber. As summarized above, extensive investigation of this sensing problem quantified the inherent difficulty in measuring power between the matching network and the powered electrode of the chamber. It was shown that both power losses and measurement accuracy scale with plasma impedance, when expressed as a standing wave ratio. As a result, measurements are *least accurate* when power losses are highest and an accurate measurement is most needed. This makes the control problem very difficult. Our research into closed-loop delivered power control led to the following conclusion: *Closed-loop delivered power control at best provides an incremental benefit at substantial cost. At worst, closed-loop delivered power control can easily result in a deterioration of process performance and increase process variability.*

Our work on RF sensing at 13.56 MHz is reported in

- C. Garvin, D. S. Grimard, and J. W. Grizzle, "RF Sensing Calibration for Real Time Control of Plasma-Based and Etching," *1998 International Conference Characterization and Metrology for ULSI Technology*, NIST, Gaithersburg, MD, March 23-27, 1998
- Garvin, C., Grimard D. S., Grizzle, J. W., and Gilchrist, B. E., "Measurement and Accuracy Evaluation of Electrical Parameters at Plasma Relevant Frequencies and Impedances," *Journal of Vacuum Science and Technology A*, Volume 16, Number 2 Mar/Apr 1998, pp 595-606.
- C. Garvin, D. S. Grimard, and J. W. Grizzle, "The Impact of Receiver Performance on the Determination of Electrical Parameters at Plasma Relevant Frequencies and Impedances", submitted to *Journal of Vacuum Science and Technology*.
- H.-M. Park, C. Garvin, D. S. Grimard, and J. W. Grizzle, "Control of Ion Energy in a Capacitively Coupled Reactive Ion Etcher," *Journal of the Electrochemical Society*, vol. 145, no. 12, pp. 4247-4252, 1999.

3.1.2 Broadband RF sensing based on plasma impedance spectroscopy

Having established the fundamental limitations on conventional approaches to plasma sensing through monitoring of the fundamental of the 13.56 RF signal, we extended our research to consider RF measurement in a more general context. One of the standard methods of approaching the problem is illustrated in Figure 19 (A). It has long been known that an RF plasma generates harmonics in the RF signal, and that these harmonics change as a function of plasma condition. However, from a control and diagnostic point

of view, the key question is not whether they change, but whether they change enough (sensitivity), and thus, whether there is sufficient information content (noise immunity) in the signal to extrapolate process-relevant information about conditions in the plasma chamber?

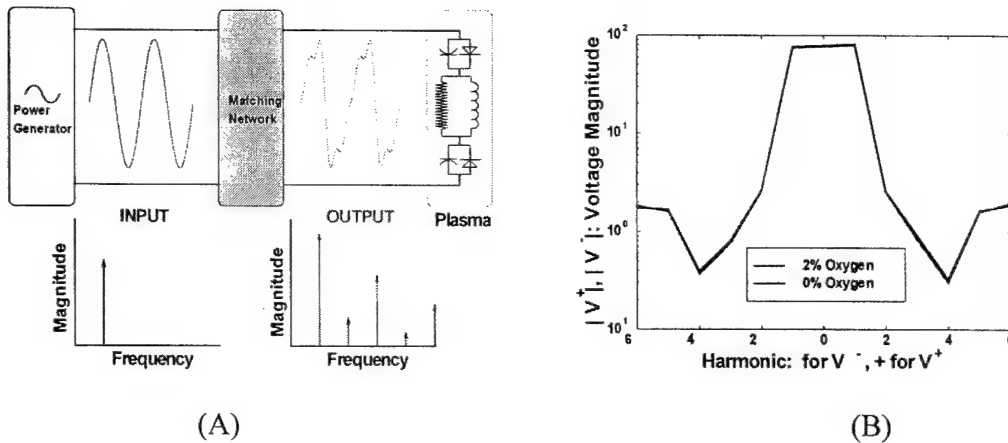


Figure 19 (A) Plasma diagnostic via harmonic content of RF signals; (B) Actual harmonic response, showing poor sensitivity. Figure 19 (B) shows the fundamental and 5 harmonics of forward and reverse voltage of the RF signal, for two different plasma chemistries (i.e., conditions). We see from the figure that standard harmonic sensing has very poor sensitivity to this type of plasma characteristic. This motivated us to consider an alternate approach to the RF diagnostic problem.

Since the early 1950's, high frequency excitation by means of a resonance probe has been used to extract parameters from ionospheric plasmas. This method is readily adaptable to a processing plasma, as shown in Figure 20 (A). A probe is inserted in the plasma and driven over a wide frequency range using a network analyzer, resulting in extremely accurate plasma measurements. The standard practice using this method has been to only determine the resonant frequency, for the purposes of estimating the plasma density. We immediately determined that there was valuable information throughout the frequency spectrum and modified the technique to capture and process the entire frequency range - thus the appellation, non-controllée, "broadband".

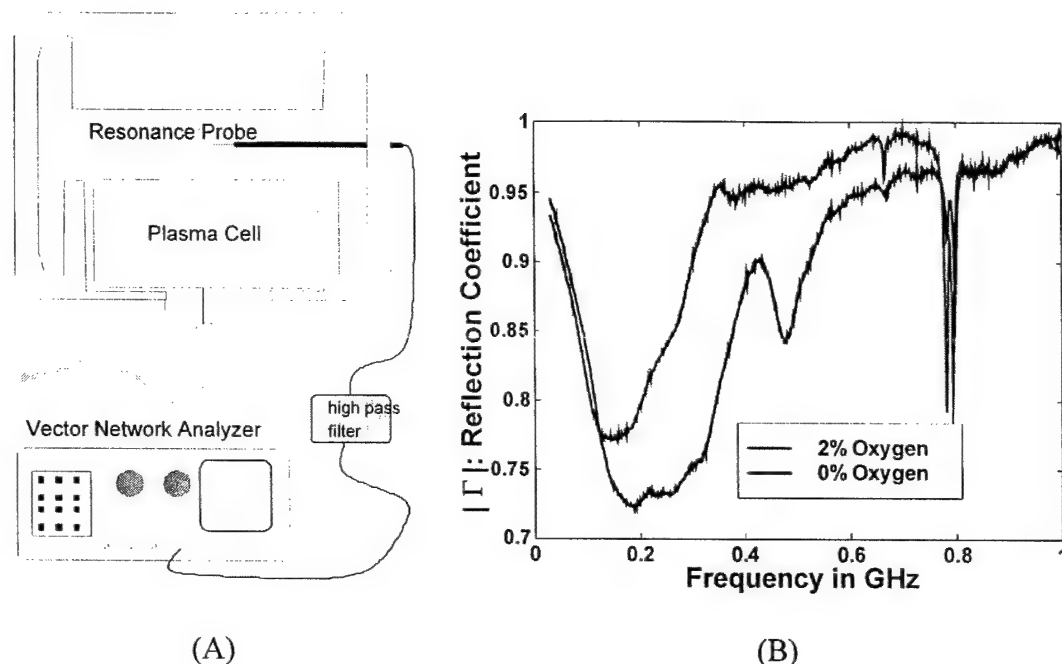


Figure 20 (A) Resonance probe implementation; (B) Resonance probe response.

The graph in Figure 20 (B) shows a plot of impedance, expressed as reflection coefficient vs. frequency, for the same two plasma conditions as before. Below about 150 MHz, the two response curves are very similar. In the range 150 to 700 MHz, the difference is very substantial. Qualitatively, at least, it appears that the “broadband” approach is more likely to provide relevant and reliable information about the process.

A relatively large-scale experiment on a research reactor was undertaken to confirm the indications of Figure 19 (B) and Figure 20 (B). The goal of the experiment was to reconstruct the power, pressure and chemistry set-points of the plasma from the measurement of broadband and (standard) narrow band (harmonic) responses, respectively. The experiments were factorial (3 factors, 3 levels), using pure Ar, pure O₂ and 50% Ar- 50% O₂ gas mixtures, pressure at 100, 175 and 250 mTorr, and power at 100, 110, and 120 Watts. 15 semi-random repetitions of the experiment were performed. The model was developed using a stepwise regression on 10 repetitions. In both broadband and narrow band data, training data was augmented by additional runs incorporating an offset equal to the measurement uncertainty in the instruments used to collect the data. This method ensured that only measurements above the uncertainty limit of the instrument were used in the fitting process.

The fit performance is determined by applying the model developed on the 10 repetitions to predict the 5 remaining repetitions. Broadband data was collected using an intrusive antenna driven by and HP8753D network analyzer over a 27.5 MHz to 2.75 GHz bandwidth. Narrow band data was obtained using a Werlatone D5281 2 MHz to 250 MHz directional coupler and HP8592L Spectrum Analyzer. Performance is summarized

in Table 2. The results of this initial experiment confirmed that the broadband sensor indeed has substantial potential as a diagnostic tool and warrants further investigation on relevant manufacturing processes.

	Pressure	Chemistry	Power
broad band	97.9 %	98.6%	83%
narrow band	65 %	88 %	76 %

Table 2 Results of initial broad band versus narrow band experiment.

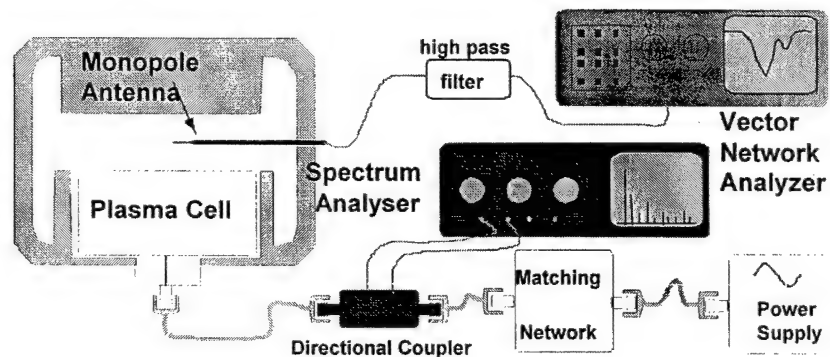


Figure 21 Experimental setup for Broadband vs. narrow band comparison

The initial test of the new sensor was followed up with the experimental setup shown in Figure 21. Plasma conditions of power, pressure and chemistry were varied in a full factorial experiment. Electrical measurements were obtained simultaneously, using both broadband and “best-of-breed” conventional narrow band sensing systems. An empirical model was regressed on half of the experimental data. This model was then employed in combination with electrical signals from the remaining experimental data to predict the plasma conditions in terms of power, pressure and chemistry. Results were dramatic. Whereas the best narrow band model achieved a best fit of $R^2 = 0.714$, averaged over the three parameters, the broadband approach achieved a nearly perfect $R^2 = 0.971$.

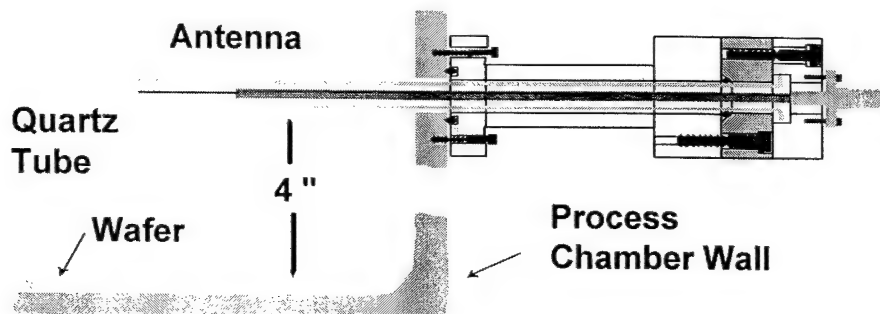


Figure 22 Processing Compatible Non-Contacting Broad Band Probe

Having established the viability of the broadband approach, we proceeded with the design of a process-compatible realization of the sensor. A new modular non-contacting system, shown in Figure 22, was designed and implemented on our Lam 9400 TCP and Plasmatherm cluster tool. A quartz tube insulates the antenna from the discharge, thus eliminating the problem of contamination. An experiment was performed in our research reactor to compare the new "non-contacting" approach to the existing "contacting" approach. The new system in fact demonstrated better sensitivity to plasma parameters than the previous "contacting" approach.

Our work on broadband RF sensing is reported in

- Garvin, C., Grimard D. S., and Grizzle, J. W., Advances in Broad Band RF Sensing for Real-Time Control of Plasma-Based Semiconductor Processing, *Journal of Vacuum Science and Technology A*, Volume 17, Number 4 Jul/Aug 1999, pp 1377-1383.
- Garvin, C., Bilen S. G., Stutzman, B. S., and Grizzle, J. W., "Implementation of Broad Band RF Sensing on a Lam 9400 Reactor", The Electrochemical Society 195th Meeting, May 2-7, 1999, Seattle, Wa.
- C. Garvin and J.W. Grizzle A Demonstration of Broadband RF Sensing: Empirical Polysilicon Etch Rate Estimation in a Lam 9400 Etch Tool, to appear in *Journal of Vacuum Science and Technology A*.

3.1.3 Fault Detection Using the Broadband Sensor

Early and accurate detection of a sensor fault is critical to decreasing semiconductor device production cost and to shortening the manufacturing cycle. Mechanical system failure is often easy to detect by visual inspection. However, sensor failure poses a much more difficult problem. An unobserved drift in the deposited power, chamber pressure, or gas flow rates can significantly impact the etch process, yet it is much more difficult to detect and identify the source of such variations. We therefore investigated the use of the Broadband Radio Frequency (RF) sensor to detect faults in the deposited Transformer Coupled Power (TCP) and pressure sensor in our Lam 9400 TCP tool. The distinctive RF fingerprint of the process from the Broadband sensor is rich enough to distinguish plasma

variations due to faults in the measurement of TCP and pressure from variation in the outputs of the remaining sensors. A non-parametric sign test was used to detect the occurrence of sensor faults on the basis of the Broadband RF signal observation.

This research was conducted using a low-pressure, high-plasma density Lam TCP 9400SE plasma etching system and an in-house-constructed Broadband RF sensor. The Broadband RF sensor consists of a 2.54-cm long tungsten probe tip inserted in an aluminum cylinder and contained in a quartz tube. A Hewlett Packard 8753B Vector Network Analyzer was used to measure the complex reflection coefficient, Γ . A 6-inch poly-Si wafer was etched under the Main Etch (ME) condition using Cl_2 and HBr gases. It was assumed that the sensor faults occur one at a time, so the five machine-input variables, TCP and Bias power, pressure, and Cl_2 and HBr flow rates, were changed one at a time from their nominal values to observe their distinctive plasma fingerprints via the Broadband RF sensor. TCP and Bias power and HBr flow rate were changed ± 10 , ± 15 , and ± 25 % from their nominal values of 250 W, 180 W, and 75 sccm, respectively. Since the pressure and Cl_2 flow rate settings are relatively small values, 10 mTorr and 15 sccm, respectively, their nominal values were changed by ± 20 , ± 30 , and ± 40 %.

3.1.3.1

Figure 23 shows a typical response of the Broadband RF sensor to a variation in TCP.

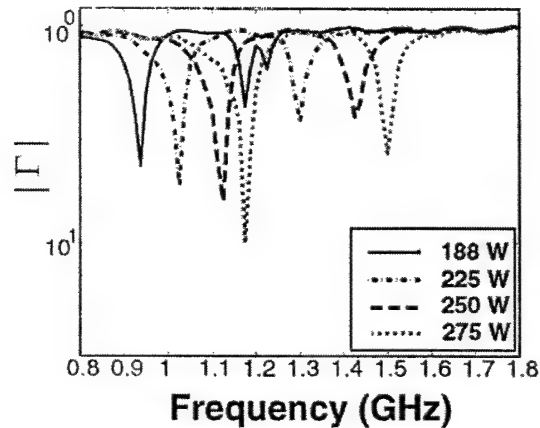


Figure 23 Variation of RF peak with TCP.

Two things can be noted: there are two dominant peaks in the reflection coefficient for each power setting, and there is a very nearly linear increase in the peak frequencies with TCP. A single sweep of the Broadband RF measurement results in 402 real numbers; 201 data points of magnitude and 201 data points of phase information of the reflection coefficient (Γ). As a first step in data reduction, an RLC circuit parameterization of the RF response was performed. Each peak of the RF response was modeled as a series RLC circuit (ω_n , Q , R) resulting in a significantly reduced data size (Figure 24).

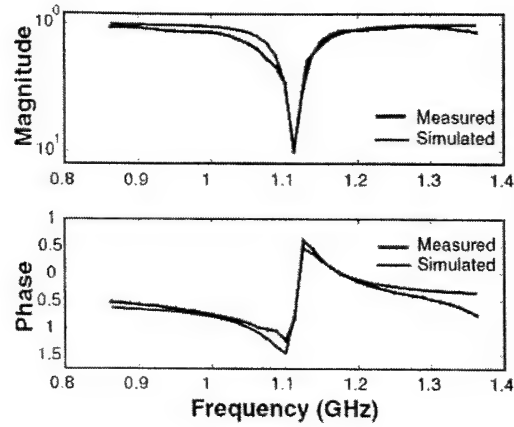


Figure 24 RLC circuit parameterization result

Next, a regression model of TCP centered about its nominal value was determined as a function of the measured RF values. A regression model was determined to be

$$TCP_{est} = 0.1985 + 0.8574\omega_{n2} - 0.6529Q_1 + 0.9510 Q_1 \omega_{n1}, \quad (1)$$

with $R^2=0.94$. Figure 25 illustrates the estimation of TCP modeled with RF sensor information. Ideally, the estimated TCP would be a straight line in the region labeled as "TCP" since only TCP was varied here. Nevertheless, the modeling error is within $\pm 5\%$. A TCP fault was declared if

$$|TCP_{nom} - TCP_{est}| / TCP_{nom} > \gamma \quad (2)$$

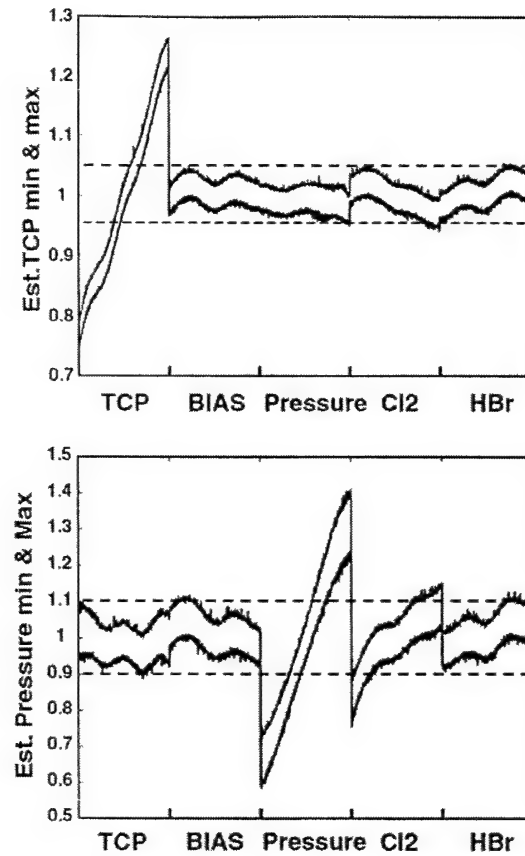


Figure 25 Normalized minimum and maximum values of the estimated TCP (top) and Pressure(bottom)

where TCP_{est} is a normalized estimated TCP value, TCP_{nom} is a normalized nominal TCP setting which is 1, and γ is a threshold to be determined. We assumed that the probability of the individual sensor error occurrence equals 10^{-4} , and that these events were mutually exclusive, and equally likely for the further calculation of the probability of detection (P_D) and probability of false alarm (P_F). Figure 26 illustrates the performance of the TCP fault detector in terms of a graph of the P_D versus P_F . The TCP fault detector provides excellent performance when TCP deviation by TCP measurement sensor error is more than $\pm 8\%$ from its nominal value. Next, the regression model of pressure was determined as

$$Pressur_{est}=0.4389+1.5931\omega_{n1}-1.6611OES+0.1451\omega_{n1}Q_1+0.4862\omega_{n2}OES \quad (3)$$

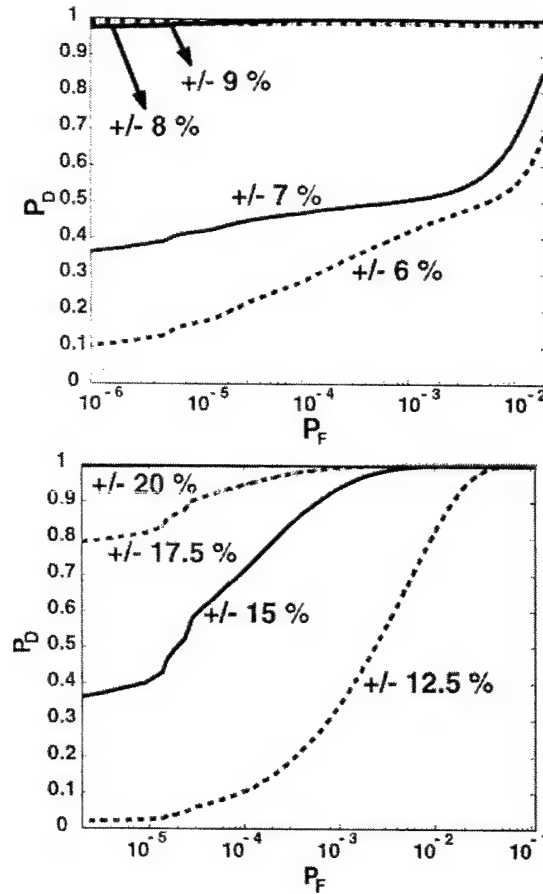


Figure 26 Receiver Operating Characteristic (ROC) of TCP (top) and Pressure (bottom) sensor fault detector.

with $R^2=0.845$. The pressure modeling error is about $\pm 10\%$ (Figure 25). A pressure fault was declared using the same form as eq. (2). A Pressure sensor fault was declared if

$$|\text{Pressure}_{\text{nom}} - \text{Pressure}_{\text{est}}| / \text{Pressure}_{\text{nom}} > \gamma \quad (2)$$

More than $\pm 20\%$ (± 2 mTorr in this study) deviation caused by the pressure sensor fault could be detected with near perfection: $P_D=0.99$ when $P_F=10^{-4}$. To check the robustness of the TCP and pressure sensor fault detector, a validation experiment was performed 5 months later in the same etching system (Figure 27). Two false alarms of pressure sensor fault detection occurred when chlorine flow rate was low. This was due to the modeling error of pressure estimation. Overall, fault detection utilizing the Broadband RF sensor was proven an accurate and reliable method for the TCP and pressure sensors.

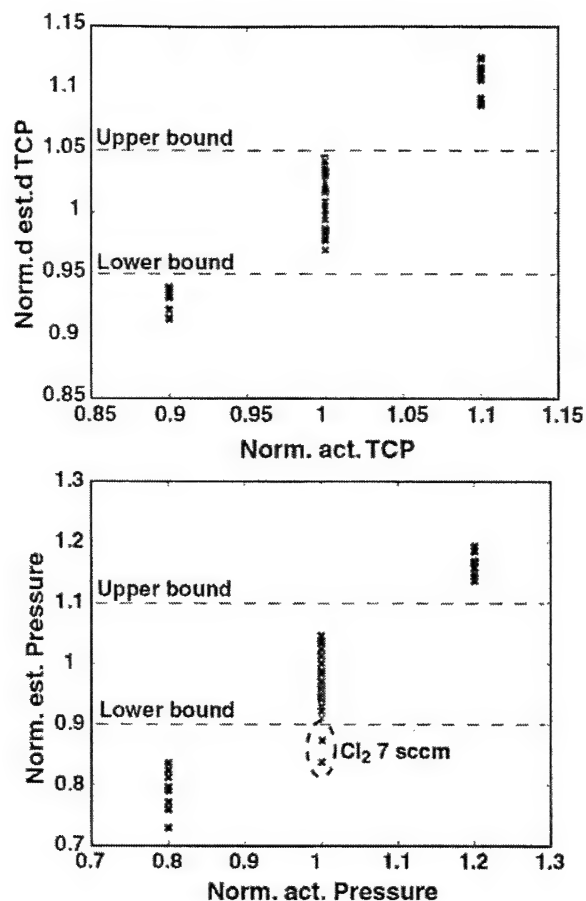


Figure 27 TCP and Pressure sensor fault detector validation experimental result.

This work was reported in

- Hyun-Mog Park, Dennis S. Grimard, Jessy W. Grizzle, and Fred Lewis Terry, Jr., "Etch profile control of high-aspect, deep submicron a-Si gate etch," *IEEE Transactions on Semiconductor Manufacturing*, **14**, pp 242-254 (2001)..

3.2 Wafer State Sensing

3.2.1 Introduction

Under funding from this program and the end of our SRC program, we independently developed and made the first open, referred publication on the use of specular-mode, spectroscopic reflected light measurements from gratings for the extraction of critical dimensions and detailed topography.¹ Similar work was being carried out in proprietary industrial laboratories² unknown to us at that time. Since these early results, this area has exploded into a significant metrology area in the Si integrated circuit industry and this method is being employed now as an in-line metrology technique for wafer-by-wafer process control.^{3,4,5,6}

Under funding from this MURI program, we demonstrated the 1st and (at this writing) still the only applications of this method to real-time, *in situ* monitoring of fabrication processes (in our case, reactive ion etching). We also performed the 1st and only experiments to control the etch of structure to a final target critical dimension value.^{7,8,9} The control/signal processing methods used to achieve these results will be described in section 4.1. In this section, we will review the physics of the topography extraction method including advances made since the last annual report.

3.2.2 Topography Extraction Example: Photoresist Lines

We have experimentally investigated a number of ~350 nm structures using wafers with large area 700 nm photoresist gratings on 31.7nm of Si on a single crystal Si wafer.

The refractive index vs. wavelength of the photoresist was extracted from a similarly processed unpatterned film using spectroscopic ellipsometry at 4 angles of incidence (60, 65, 70, 75°) to reduce the artifacts produced at antireflection points. The period of the grating was verified by measuring the angle of the 1st order diffraction peak as a function of wavelength under an illumination angle of 7°. This data was fit to the classic grating equation:

$$\sin(\theta_d) = \frac{m\lambda}{\Lambda} + \sin(\theta_i)$$

where Λ is the grating period, λ is the wavelength, θ_i is the angle of incidence, θ_d is the angle of diffraction, and m is the diffraction order ($m=1$ for the Λ extraction). This extraction and an SEM photo of a representative grating are shown in Figure 28.

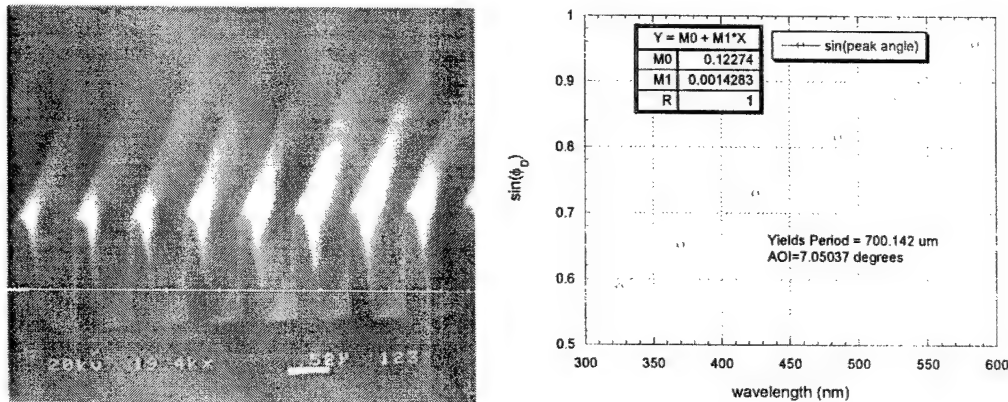


Figure 28 SEM cross-sectional image of 350 nm line/space grating on 31.7nm of SiO₂ on Si (left). The grating period was verified to be 700.14±0.33nm using measured 1st order diffraction peaks vs. wavelength with an illumination angle of 7° and fits to the grating equation (right figure).

Ex situ spectroscopic ellipsometry measurements were collected using a Sopra GESP-5 rotating polarizer ellipsometer with a photomultiplier/high-resolution scanning

monochromator detection system. Data were collected at 7, 63.5, and 73° AOI's for comparison with *in situ* data from etch systems. For this sample, the near-normal configuration proved to be the most sensitive, so only that data will be shown in this paper. In other sample cases, AOI's ~60-75° may prove to be advantageous.

The data from both our *ex situ* and *in situ* measurements were fit using parameterized geometric models for the lineshape, rigorous coupled wave analysis (RCWA) for the specular scattering calculations, and Levenberg-Marquardt nonlinear regression to optimize the fit of the simulations resulting from geometric parameters vs. the measured data.

First, let us examine a simple fit using a trapezoidal model and data from the 400-800nm range. This fit is shown in Figure 29. The quality of the fit is good (though certainly shows room for improvement), and all the basic shape of the data is approximately captured by the fit. However, if the range of the measurement is extended into the UV (230-825nm), then the data and trapezoidal fit of Figure 30 result. Clearly, there is significant structure in the shorter wavelength data that is not properly captured by the simple trapezoidal fit. This is an indication that the topography is more complex. Furthermore, noting that the trapezoidal model yields sharper, larger amplitude data in the UV is an indication that the real structure is more rounded on top than the sharp, relatively wide top of the trapezoid.

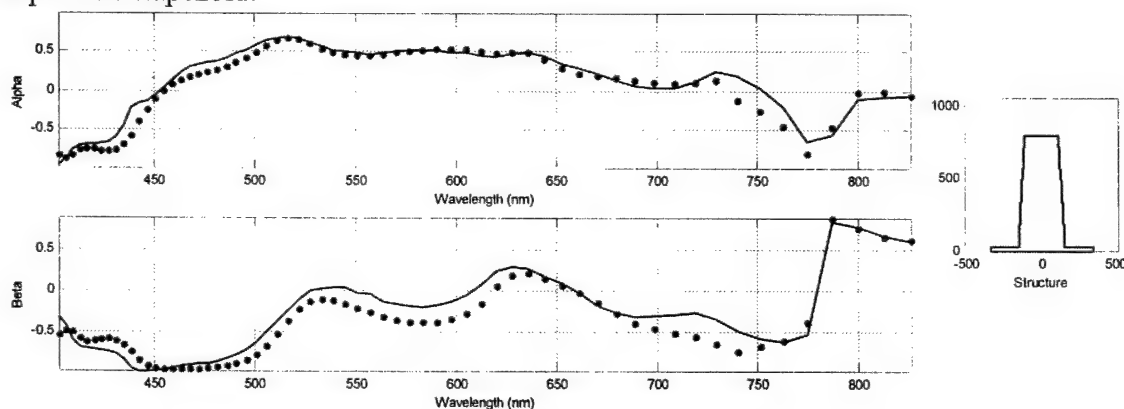


Figure 29 Measured (solid curves) and fitted (dots) results for near-normal 7° AOI spectroscopic ellipsometry data (α, β parameters) from 400-825nm. The best fit trapezoidal model is shown to the right.

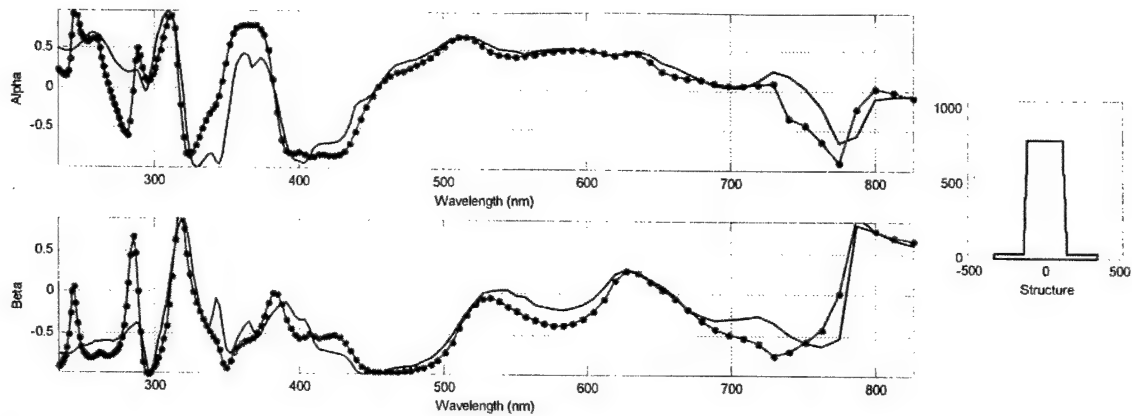


Figure 30 The data from Figure 29 now extended to 230-825nm. Note that there is significant structure in the measured data that is not captured in the fitted curves (dots).

We proceeded through a succession of geometric models: (1) a trapezoid on a rectangle; (2) a triangle on trapezoid on a rectangle; and, (3) finally a 3-segment quadratic fit (basically a "triangle" with curvature sitting on a "trapezoid" with curvature sitting on a second "trapezoid" with curvature). The final fit is shown in Figure 31. All models are overlaid in Figure 32 and the best fit is shown overlaying a cross-sectional SEM photo also in this figure.

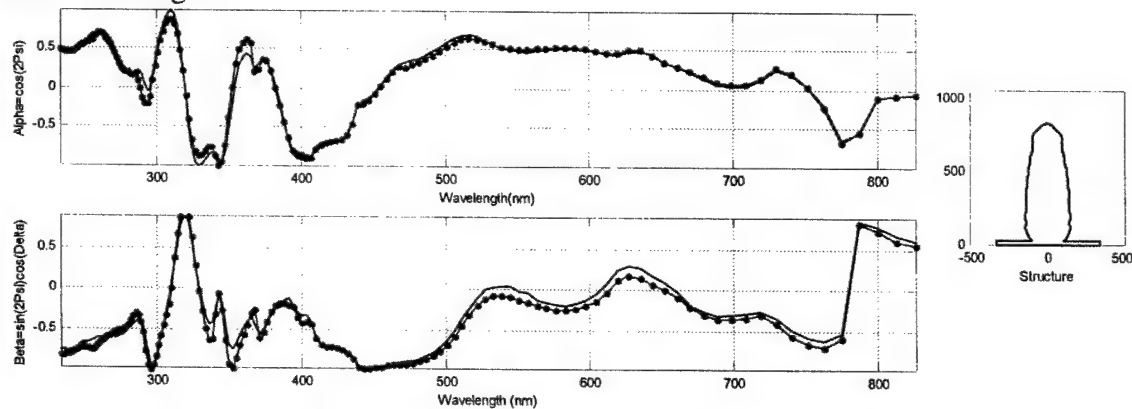


Figure 31 The same data as Figure 30 but now fit using a 3 segment, 2nd order polynomial fit of the sidewall shape. Note that nearly all of the major structures in the data are fit by this geometric model. The sources of the residual errors are not clearly, but may be related to slight variations in the refractive index of the resist line vs. the (n,k) reference data extracted from a similar blanket test sample.

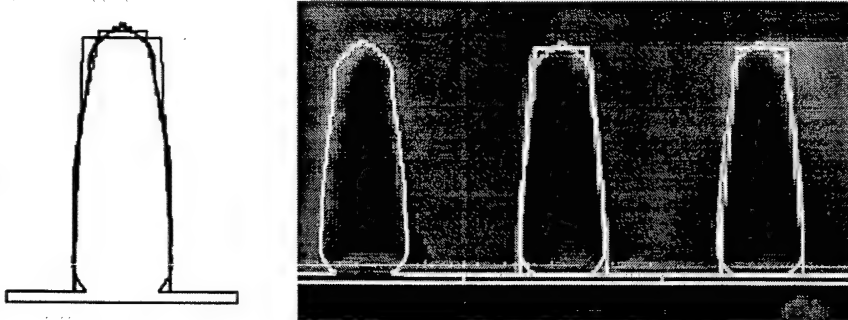


Figure 32 The results of the fit from Figure 31. The left figure shows all explored geometric models overlaid (trapezoid, trapezoid-on-rectangle, triangle-on-trapezoid-on-rectangle, and finally the 3-segment quadratic fit). The 3-segment, 2nd order fit is overlaid on the cross-sectional SEM photo. The only adjustment of image size was a constant scaling to match the measured period.

The parameters used in this fit are shown in Table 3. For each fitted segment j , the width of segment at a given point y measured down from the top of the segment is given by:

$$w(y) = \left[m_{j0} + m_{j1} \left(\frac{y}{h_j} \right) + m_{j2} \left(\frac{y}{h_j} \right)^2 \right] \Lambda$$

For this fit, we set $m_{10}=0$ for the top curved triangle. This was done since attempts to extract a top width yielded numbers which were essentially zero and which had no statistical significance. The remaining m_{j0} 's were linked to the bottom width of the segment above so that the sidewall structure was a continuous function of y . For this fit, this results in 9 independent parameters. The standard 95.5% confidence limits for this fit are also shown in the table. All of the fitted parameter show confidence limits that are less than the parameters themselves, indicating that all have some statistical validity in the topography extraction. However, the cross correlation coefficients are examined (Table 4), we see that there is strong coupling between the heights of the main middle segment (h_2) and the height of the lower undercut segment (h_3). Also, we see strong coupling between the slope and the curvature of the main segment (m_{21} & m_{22}). The latter correlation is not too surprising as the middle segment is close to vertical, and thus resolution of the slight curvature is difficult. The h_2 - h_3 correlation illustrates the difficulty in clearly resolving the slight undercut. In summary for this point, we have now pushed this data to the limit of statistical merit. Further parameterization could improve the quality of fit, but would not result in topographic parameters for which we could be physically confident.

Table 3 Extracted parameters for the fits shown in Figure 31 and Figure 32.

Term	Value	95.4% conf. Limit	Units
h1	146.51	4.55	nm
m11	0.7389	0.0097	slope
m12	-0.4698	0.011	quadratic curvature
h2	545.72	36.05	nm
m21	0.3461	0.0272	slope
m22	-0.1921	0.0282	quadratic curvature
h3	112.35	34.79	nm
m31	0.0803	0.0529	slope
m32	-0.1933	0.0659	quadratic curvature

Table 4 Cross-correlation coefficients for the parameter in Table 3. The cross-correlations above 0.9 indicate cause for concern in over-fitting of the data.

	h1	m11	m12	h2	m21	m22	h3	m31	m32
h1	1	0.356	-0.217	-0.369	-0.176	0.121	0.267	0.101	0.04
m11	0.356	1	-0.88	-0.34	-0.31	0.354	0.301	-0.098	0.219
m12	-0.217	-0.88	1	0.373	-0.02	-0.08	-0.363	-0.146	-0.009
h2	-0.369	-0.34	0.373	1	0.512	-0.527	-0.993	-0.369	-0.108
m21	-0.176	-0.31	-0.02	0.512	1	-0.981	-0.493	0.286	-0.474
m22	0.121	0.354	-0.08	-0.527	-0.981	1	0.517	-0.31	0.501
h3	0.267	0.301	-0.363	-0.993	-0.493	0.517	1	0.394	0.082
m31	0.101	-0.098	-0.146	-0.369	0.286	-0.31	0.394	1	-0.866
m32	0.04	0.219	-0.009	-0.108	-0.474	0.501	0.082	-0.866	1

In situ measurements and real-time control experiment were conducted using these samples. A Lam 9400 TCP SE poly Si etch system was slightly modified to add ports for ellipsometry. Due to vacuum system constraints, the AOI was 63.5°. Spectroscopic ellipsometry data was collected using a Sopra RTSE (real-time spectroscopic ellipsometer) which is a rotating polarizer SE with a prism spectrometer/CCD array detector for high speed data acquisition. This system allows data collection at a 180 ms sampling rate. The SE measurement itself occurs in 100ms. This fast data collection rate allows each measurement to be treated as a quasi-static snap shot of the sample. The gratings in these test were rotated so that the plane of incidence was perpendicular to the grating. Representative data from these measurements is shown in Figure 33.

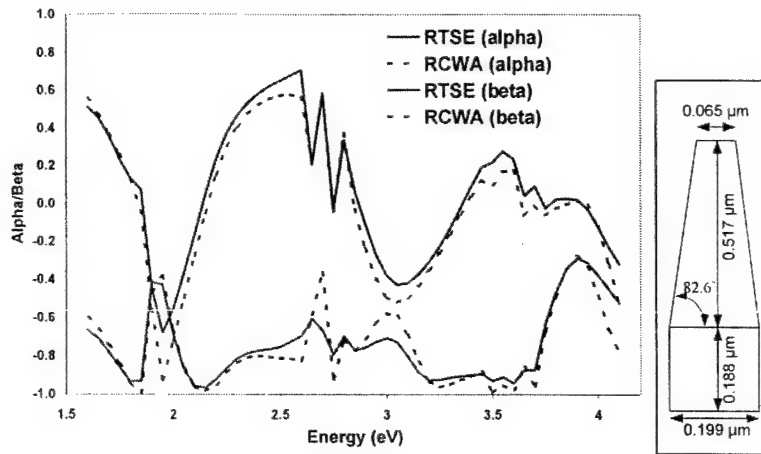


Figure 33 Representative data from the in situ RTSE measurements of the photoresist grating. Measured data and regression fits are shown (left) and the resulting topography fit (trapezoid on rectangle model) is shown on the right.

We used an O_2 plasma to trim-back the photoresist lines. A small library of SE simulations vs. geometries around the expected topography trajectory was used to determine the coefficients of a convex-hull-based nonlinear filtering algorithm (NLF). This NLF is a sort of pattern matching approach with some robustness to noise and experimental data distortions. It allowed rapid topography extraction (~ 0.25 s on a 600MHz PIII PC) during the trim-back step. Automatic endpoint was triggered for the desired trim-back to 200 nm bottom CD. The before and after cross-sections resulting from this run are shown in Figure 34. This trapezoid on rectangle fit yield a starting condition of 296 nm bottom CD, 169 nm top CD, an 84.2° upper segment sidewall angle and a total line height of 777 nm. The final structure has a 200 nm bottom CD, 71nm top CD, and 82.1° upper segment sidewall angle, and a total line height of 697 nm. A "movie" of this process can be viewed on the website http://www.eecs.umich.edu/~fredty/spie2003/sprt7_tritraprect.mov (Quicktime).

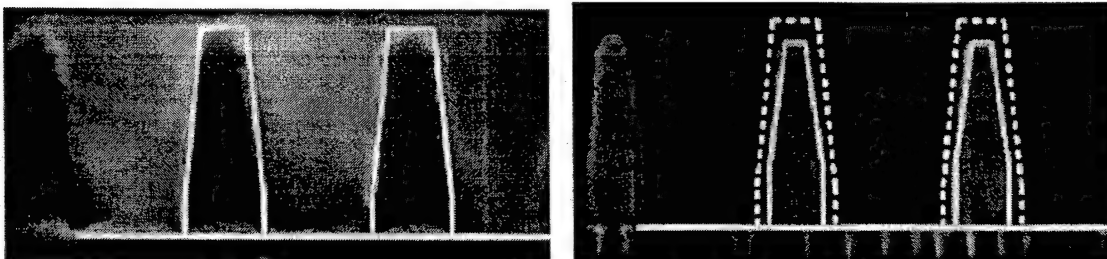


Figure 34 Real-time, in situ spectroscopic ellipsometry extractions of beginning photoresist shape (left) and post-trim-back photoresist shape over-laid with cross-sectional SEM photos.

Close examination of the post trim-back photo shows that there is slight undercut of the photoresist line. However, if we attempt to extract this additional feature detail from the RTSE data, we obtain a physically unreasonable total line undercut (just a few 10's of nm

on the bottom) and much larger confidence limits than the fitted parameters themselves. This limited accuracy condition arises because

1. The RTSE data is more limited in wavelength (shortest usable wavelength $\sim 300\text{nm}$) than the *ex situ*, scanning system measurements;
2. The RTSE data is somewhat distorted due to stray light effects in the prism spectrometer which reduce the intensity and sharpness of the structure of the (α, β) data.

The wavelength limitation issue is qualitatively obvious, but further work will be required to quantitatively understand the resolution limits of this measurement technique. This will be area of continuing research interest. The distortion issue in using the RTSE data was one of the primary reasons that sophistication was required in the signal processing/control methods for making use of this data for endpoint detection. This methods will be discussed in section 4.1.

3.2.3 Challenges and Future Work

Specular mode, spectroscopic reflected light measurements (sometime called specular scatterometry) have moved rapidly from the research world to industrial application. These methods are being used presenting in integrated circuit fabrication control on an in-line/wafer-to-wafer basis. In that regard, it is an major success which has at least partially been pushed forward by this program. However, several fundamental issues still remain:

1. Developing a quantitative understanding of the resolution limitation of various possible extraction and measurement modes.
2. Developing practical method for measurement of aperiodic structures and the extension of real-time results demonstrated under this program to product wafers (for true real-time, in situ control of topography).
3. Pushing the resolution limits into the true nano-scale regime.
4. Developing measurement methods for sparse (isolated) structures.

3.2.4 References

-
- ¹ "Analysis of reflectometry and ellipsometry data from patterned structures," M.E. Lee, C. Galarza, W. Kong, W. Sun, and F. L. Terry, Jr., Characterization and Metrology for ULSI Technology. 1998 International Conference. 23-27 March 1998; Gaithersburg, MD, USA, AIP-Conference-Proceedings. no.449; 1998; p.331-5.
 - ² E. W. Conrad, D. P. Paul, US Patent 5,963,329 filed Oct. 31, 1997.
 - ³ "Spectral scatterometry for 2D trench metrology of low-k dual-damascene interconnect," V. A. Ukraintsev, M. Kulkarni, C. Baum, K. Kirmse, Texas Instruments Inc.; M. Guevremont, S. Lakapragada, K. N. Bhatia, P. P. Herrera, U. K. Whitney, KLA-Tencor Corp., SPIE Conference on Metrology, Inspection, and Process Control for Microlithography XVI, Santa Clara, CA, March 4-7, 2002.
 - ⁴ "Fundamental solutions for real-time optical CD metrology," J. Opsal, H. Chu, Y. Wen, G. Li; Thermo-Wave, Inc., SPIE Conference on Metrology, Inspection, and Process Control for Microlithography XVI, Santa Clara, CA, March , 4-7, 2002.
 - ⁵ "Spectroscopic optical metrology for process characterization and control," J. Allgair and P. Herrera, Microlithography-World. vol.11, no.1; Feb. 2002; p.12, 14, 16, 23-4

-
- ⁶ "Specular spectroscopic scatterometry," Niu Xinhui, N Jakatdar, Junwei-Bao, C.J. Spanos, IEEE-Transactions-on-Semiconductor-Manufacturing. vol.14, no.2; May 2001; p.97-111.
- ⁷ Hsu-Ting Huang, Ji-Woong Lee, Brooke S. Stutzman, Pete Klimecky, Craig Garvin, Pramod P. Khargonekar, and Fred L. Terry, Jr., "Real Time In Situ Monitoring of Deep Sub- μ m Topography Evolution during Reaction Ion Etching," SEMATECH AEC/APC Symposium, Lake Tahoe, NV., September 25-28, 2000. (One of 4 best student paper awards at this conference)
- ⁸ Hsu-Ting Huang, Brooke S. Stutzman, Wei Kong, Pete Klimecky, and Fred L. Terry, Jr., "Real Time In Situ Observation of Deep Submicron Topography Evolution Using Spectroscopic Ellipsometry and Reflectometry," AVS International Conference on Metallic Coatings and Thin Films (ICMCTF), San Diego, CA., May 1, 2001. (invited talk by Fred Terry)
- ⁹ 2. "In Situ Monitoring Of Deep Sub-mm Topography Evolution And Endpoint Detection During Reactive Ion Etching," Hsu-Ting Huang, Ji-Woong Lee, Pete Klimecky, Pramod P. Khargonekar, and Fred L. Terry, Jr., SEMATECH AEC/APC Symposium XIII, October 6-11, 2001, Banff, Alberta, Canada

4 Control

4.1 Real-Time State Estimation for Patterned Wafers

4.1.1 Introduction

Real-time estimation and control of semiconductor wafer topography is becoming increasingly crucial as pattern dimensions of modern integrated circuits continuously shrink. Our work is concerned with the problem of real-time estimation of the profile of a periodic grating during plasma etching with optical observation. Difficulties in this problem are that no control-oriented dynamic models for plasma etching are available, and that the existing observation model is of high computational complexity. Due to these difficulties, standard approaches such as extended Kalman filtering cannot be applied.

Our approach is to develop a new state estimation technique that overcomes unknown dynamics and computationally complex observation. We propose a nonlinear filtering algorithm for unknown dynamics, and high-complexity, high-dimensional observation. Experimental results with the proposed algorithm include the first reported successful real-time monitoring of, and end point detection for, patterned wafer topography evolution during plasma etching. The algorithm is shown to produce state estimates with bounded error under bounded disturbances and redundant observations, and to reduce to the maximum *a posteriori* probability estimator under an ideal case. Finally, a version of the proposed algorithm is used to obtain angle of incidence-free real-time wafer state estimates.

4.1.2 Motivating Problem and Previous Work

Reactive ion etching (RIE) is an important plasma etching technique commonly used in VLSI and ULSI fabrications. However, the underlying physics and chemistry in RIE are known to be very complex and multi-variable, and they are not very well understood. In fact, no control-oriented physics based dynamic models for the patterned-wafer topography evolution during RIE are not currently available. On the other hand, since the process should not be disturbed, many of the crucial parameters cannot be directly measured in real time, so, for real-time estimation and control of patterned wafer

parameters, the RIE process needs to be coupled with a non-destructive *in situ* sensor that is sensitive to etch parameters.

Optical measurement techniques such as spectral reflectometry and spectroscopic ellipsometry are the most favorable techniques for indirectly determining the surface properties of a sample being processed because of their non-destructive nature and sensitivity, and have become widely used methods in various applications. Consider the situation where a light beam is incident to a sample surface at a fixed incidence angle. According to elementary optics, after reflection on a sample surface, a linearly polarized single-wavelength light beam, with wavelength λ , becomes elliptically polarized resulting in complex reflection coefficients $R_p(\lambda)$ and $R_s(\lambda)$. One of our optical *in situ* sensors, the Two Channel Spectroscopic Reflectometer (2CSR)¹⁰, measures $|R_p(\lambda)|^2$ and $|R_s(\lambda)|^2$ over multiple wavelengths λ to extract the properties of a patterned surface.

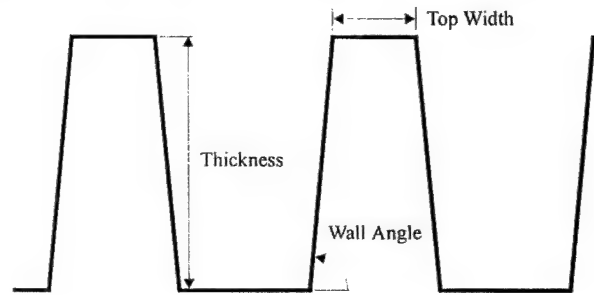


Figure 35 Trapezoidal periodic grating

We are focused on the RIE process on a photoresist grating with the 2CSR observation. As in Figure 35, the profile of a photoresist grating is approximated to be trapezoidal. In this case, given the grating period, the wafer state x_k at time k is defined to be the triplet of Thickness, Top Width, and Wall Angle. The measured 2CSR output z_k at time k is the 2ℓ -tuple of $|R_p(\lambda_1)|^2$, $|R_s(\lambda_1)|^2$, ..., $|R_p(\lambda_\ell)|^2$, $|R_s(\lambda_\ell)|^2$, when ℓ wavelengths λ_1 , ..., λ_ℓ are considered. Let $X \subset \mathbf{R}^3$ be the space of all possible wafer states. Then a function $h: X \rightarrow \mathbf{R}^{2\ell}$, such that $h(x)$ is the model output corresponding to a wafer state $x \in X$, is obtained from the rigorous coupled wave analysis (RCWA)¹¹. The function h is not in a closed analytic form, but rather given by a complex numerical code, so the

computational demand of the RCWA model is very high, and direct use of h is impossible in real-time applications. Indeed, given x_k , evaluation of the model output $y_k = h(x_k)$ takes up to a minute on a high-end workstation; on the other hand, given z_k , the nonlinear least squares model fitting that minimizes $\|z_k - h(x)\|$ over $x \in X$ takes about 15 minutes on the same machine.

In the case of unpatterned wafers, one can use a low-complexity optical observation model, and real-time etch rate estimation is possible via extended Kalman filtering with a random-walk approximation of the etch rate evolution¹². However, in the case of patterned wafers, due to the high computational complexity of the RCWA model, the common practice has been to assume that the dynamics is completely unknown and resort to *ex situ* nonlinear least squares model fitting to extract the wafer state trajectory^{13,14}. Although low-complexity approximation of the RCWA model has been attempted using neural network models trained with simulated data¹⁵, there has been no reported experimental validation of such an approximate model. On the other hand, empirical modeling of the 2CSR observation¹⁶ has turned out to be of limited applicability due to the huge number of experimental data required to train a neural network.

4.1.3 Problem Formulation

Let $X \subset \mathbf{R}^n$ be the state space. Consider the discrete-time state space model

$$\begin{aligned}x_{k+1} &= f_k(x_k) + w_k, \\z_k &= h(x_k + v_k) + e_k, \\k &= 0, 1, \dots,\end{aligned}$$

where $x_k \in X$ is the state and $z_k \in \mathbf{R}^m$ is the output at time k . The functions f_k are unknown, and the function h cannot be evaluated in real time; w_k are input disturbances, v_k represent a part of systematic errors in modeling, and e_k define the deviation of the measured outputs z_k from the model outputs $y_k = h(x_k + v_k)$ due to measurement noise as well as the modeling errors that are not taken into account by v_k .

Since f_k are unknown, we use approximations of them, either given at the outset or determined from data. For each k , fix a mapping \mathcal{F}_k that maps the observation sequence $z^k = (z_0, \dots, z_k)$ into the space of functions from X into \mathbf{R}^n . Then the collection $\{\mathcal{F}_k\}$ is a subsidiary filter that determines an approximation $\hat{f}_k = \mathcal{F}_k(z^k)$ of f_k for each k . On the other hand, since h cannot be directly used, we construct a sampled version of it as follows. Choose a finite set D whose points form a uniform grid on X . Then D defines a finite number of closed boxes R_1, \dots, R_p of the same size such that $R_i \cap D$ is the set of vertices of R_i for each i . By offline model simulation, we obtain a sample \mathcal{H}_D of h given by $\mathcal{H}_D = \{(d, h(d)) : d \in D\}$.

Now, our filtering problem is as follows: given $\{\mathcal{F}_k\}$ and \mathcal{H}_D , get an estimate $\hat{x}_{k|k}$ of x_k (and a prediction $\hat{x}_{k+1|k}$ of x_{k+1}) based on z^k for each k . Any technique tackling this problem should be capable of dealing with unknown dynamics and computationally complex observation.

4.1.4 Proposed Filtering Algorithm

We propose that the filtering algorithm consist of the following steps at each time k : to derive an estimate \hat{y}_k of the model output y_k ; to find a function \hat{h}^{-1} , which contains \hat{y}_k in its domain, such that $\hat{h}^{-1}(\hat{y}_k) \in h^{-1}(\{\hat{y}_k\})$ whenever $\hat{y}_k \in h(X)$, and to evaluate $\hat{h}^{-1}(\hat{y}_k)$; to obtain an estimate $\hat{x}_{k|k}$ of x_k by compensating for the systematic error v_k from $\hat{h}^{-1}(\hat{y}_k)$; to make a prediction $\hat{x}_{k+1|k}$ of x_{k+1} . The following algorithm has this structure. (For $S \subset \mathbf{R}^n$, denoted by $\text{conv}(S)$ is the convex hull of S .)

Algorithm A.

Step 0. Fix boxes $\hat{W}, \hat{V} \subset \mathbf{R}^n$; make a prediction $\hat{x}_{0|-1}$ of x_0 ; let $\hat{X} = \hat{x}_{0|-1} + \hat{W}$; set $k = 0$.

Step 1. Get z_k ; determine \hat{f}_k from z^k .

Step 2. Let $D_k = (\hat{X}_k + \hat{V}) \cap D$.

Step 3. Compute $\hat{y}_k = \arg \min \{\|y - z_k\| : y \in \text{conv}(h(D_k))\}$, and obtain $\{\lambda_d\}_{d \in D_k}$ such that $\sum_{d \in D_k} \lambda_d = 1$, $\lambda_d \geq 0$, and $\hat{y}_k = \sum_{d \in D_k} \lambda_d h(d)$.

Step 4. Let $\hat{h}^{-1}(\hat{y}_k) = \sum_{d \in D_k} \lambda_d d$, and compute $\hat{x}_{k|k} = \arg \min \{\|x - \hat{x}_{k|k-1}\| : x \in \hat{h}^{-1}(\hat{y}_k) - \hat{V}\}$.

Step 5. Set $\hat{x}_{k+1|k} = \hat{f}_k(\hat{x}_{k|k})$, and $\hat{X}_{k+1} = \hat{x}_{k+1|k} + \hat{W}$.

Step 6. Increment k to $k+1$; go to Step 1.

In Algorithm A, Steps 1-4 correspond to the measurement update step of nonlinear filtering: the set D_k determines the constraint sets for the optimization steps that follow Step 2; the two optimization steps, Step 3 and Step 4, are coupled through the choice of \hat{h}^{-1} and evaluation of $\hat{h}^{-1}(\hat{y}_k)$. Step 5 is the time update step: the function \hat{f}_k is used to predict next state; the box \hat{X}_k is evolved into \hat{X}_{k+1} , so that it is used to update D_k into D_{k+1} at time $k+1$.

4.1.5 Experimental Results

Algorithm A has enabled us to achieve the first reported real-time state estimation for sub-micron patterned wafers during plasma etching¹⁶. Assuming that the etch rate is sufficiently low, let $\hat{f}_k(x) = x$ for all x ; for simplicity, let $\hat{V} = \{0\}$. Using the trapezoidal approximation of the grating profile as in Figure 35, and choosing 46 wavelengths from the spectral range of the 2CSR outputs, we have $n = 3$ and $m = 92$.

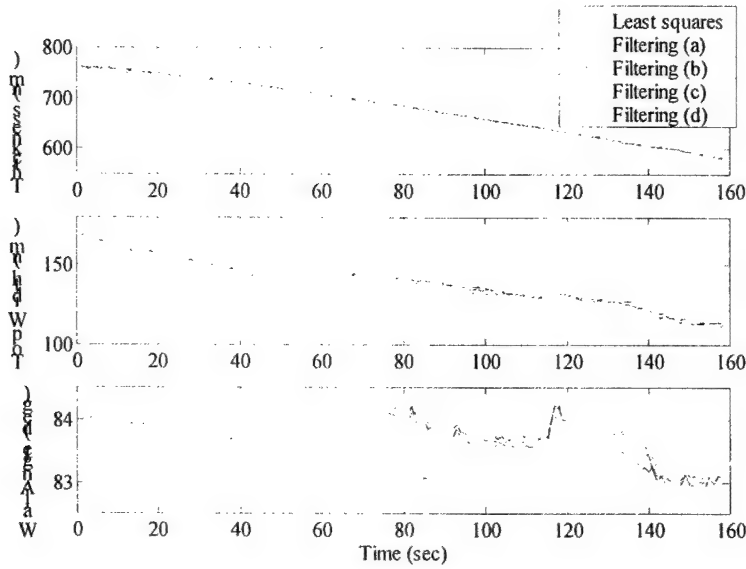


Figure 36

Figure 36 shows a typical real-time wafer state estimation result obtained using Algorithm A during an RIE process for a photoresist grating. For reference, marked by x 's are the offline nonlinear least squares fits. For boxes $S \subset \mathbf{R}^n$, denote the j -th side-length of S by $\text{len}_j(S)$, $j = 1, 2, 3$; let $\text{len}_j(R_1) = l_j$. Four different sets of wafer state estimates are produced with four different choices of \hat{W} : (a) $\text{len}_j(\hat{W}) = 3l_j$ (solid lines); (b) $\text{len}_j(\hat{W}) = 2l_j$ (dotted lines); (c) $\text{len}_j(\hat{W}) = 4l_j$ (dash-dotted lines); (d) $\text{len}_j(\hat{W}) = 5l_j$ (dashed lines). Among (a)-(d), choice (a) is the only one that is within the range of \hat{W} expected to yield good wafer state estimates according to the analysis result we will give in Section 6. Indeed, the estimates produced by choice (a) are the closest to the nonlinear least squares results—the real-time estimates of Thickness, Top Width, and Wall Angle given by the solid lines are uniformly within 5 nm (1 %), 5 nm (3 %), and 0.5° (0.5 %), respectively, of the least squares fits.

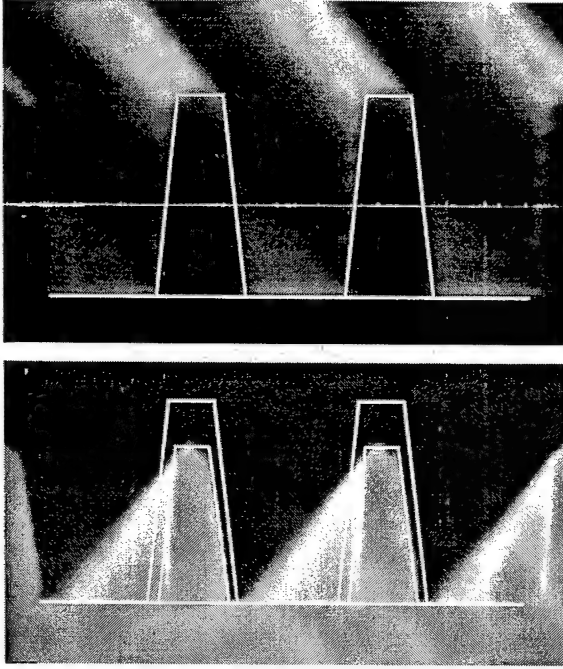


Figure 37 Left (a) is a sample cross-section and trapezoidal fit before the etch. Right (b) is the cross-section after the trim-back etch with the before and after trapezoidal fits.

Algorithm A has also enabled us to achieve successful end point detection results^{16,17}. The cross-section scanning electron microscope (SEM) photos demonstrating such a result is shown in Figure 37. The bottom width of the photoresist grating is considered to be the critical dimension. The bottom width of 250 nm is targeted, and an RIE process for a photoresist grating is terminated at time k once the real-time wafer state estimate $\hat{x}_{k|k}$ leads to a bottom width less than or equal to the target bottom width. Figure 37(a) shows the SEM photo from a part of the sample before the RIE process and the estimated profile at the beginning of the etching. Figure 37(b) shows the SEM photo after the RIE process and the estimated grating profile from Algorithm A at the end of etching. In this example, the end point estimates of the bottom width from Algorithm A and nonlinear least squares model fitting are 249 nm and 251 nm, respectively. They are in good agreement with the SEM photo although there are some ghost images and shining lines due to the space charging effects of the SEM.

4.1.6 Analysis Results

A generalized version of Algorithm A has been analyzed in [18] and shown to be stable—that is, to produce state estimates with bounded error—under certain conditions. In particular, it can be shown that Algorithm A is stable under the following assumption:

Assumption A.

- (a) The state space X is compact; there are $\lambda_k \geq 0$ such that $\|f_k(x) - f_k(\tilde{x})\| \leq \lambda_k \|x - \tilde{x}\|$ for all k and all $x, \tilde{x} \in X$.
- (b) There are $\varepsilon_k \geq 0$, and compact $X_0, W_k, V_k \subset \mathbf{R}^n$ such that $x_0 \in X_0, w_k \in W_k, v_k \in V_k$, and $\|e_k\| \leq \varepsilon_k$ for all k .
- (c) For each $R_i, i \in \{1, \dots, p\}$, there exist $A_i \in \mathbf{R}^{m \times n}$ and $a_i \in \mathbf{R}^m$ such that $h(x) = A_i x + a_i$ for $x \in R_i$.
- (d) Let ρ be the largest integer satisfying the following: whenever $i_1, \dots, i_\rho \in \{1, \dots, p\}$ are such that $\bigcup_{j=1}^\rho R_{i_j}$ is connected and $\{A_{i_1}, \dots, A_{i_\rho}\} = \{A_{i_1}, \dots, A_{i_q}\}, q \leq \rho$, with $A_{i_j} \neq A_{i_k}$ for $j < k \leq \rho$, the matrix $[A_{i_1} \cdots A_{i_q}] \in \mathbf{R}^{m \times qn}$ has full rank. Then $\rho \geq 3$.
- (e) There exist compact $F_k \subset \mathbf{R}^n$ such that $f_k(x) - \hat{f}_k(x) \in F_k$ for $x \in X$.
- (f) For simplicity, let $V_k = \hat{V} = \{0\}$; for $q \leq \rho$, let \mathcal{A}_q be the set of matrices $[A_{i_1} \cdots A_{i_q}]$ where i_1, \dots, i_q are as in (d); let \mathcal{M}_ρ be the set of $\sum_{k=1}^q B_k$ over $q \leq \rho, \mathcal{A} \in \mathcal{A}_q$, and $(A^T A)^{-1} A^T = [B_1^T \cdots B_q^T]^T$; let $\mu = \max\{\|B\|: B \in \mathcal{M}_\rho\}$. Then the sets $-\hat{x}_{0|-1} + X_0$ and $\lambda_k \text{Ball}(\mu \varepsilon_k) + F_k + W_k$ are contained in the box centered at the origin and of the same size as R_1 . (For $\varepsilon \geq 0$, $\text{Ball}(\varepsilon)$ denotes the closed ε -ball centered at the origin.)
- (g) The box \hat{W} is centered at the origin with $3l_j \leq \text{len}_j(\hat{W}) < 4l_j, j = 1, 2, 3$.

Assumption A(a) says that the functions f_k are Lipschitz continuous on the compact state space, and Assumption A(b) says that the disturbances are all bounded. The function

h is piecewise linear and continuous, and each piece of h is defined by Assumption A(c); that is, we replace the “true” h with a piecewise approximation of it, and let any error incurred in doing so be absorbed in either v_k or e_k . We call the number ρ defined in Assumption A(d) the “redundancy number” of h ; $\rho > 0$ implies that at least each piece of h is one-to-one, and $\rho \geq 3$ implies that the inequality $m \geq n3$ is likely to hold (as long as h is not intentionally made to be very simple). Assumption A(e) says that \hat{f}_k are approximations of f_k with bounded error, and Assumption A(f) says that the underlying disturbances and errors are small. Finally, Assumption A(g) says that the box \hat{W} is sufficiently large and sufficiently small at the same time.

Lemma A.

If Assumption A(c) holds with $\rho > 0$, and if $i_1, \dots, i_\rho \in \{1, \dots, p\}$ are such that $U = \bigcup_{j=1}^\rho R_{i_j}$ is connected, then there exist $B \in \mathbf{R}^{n \times m}$ and $b \in \mathbf{R}^n$ such that the function $\phi: \text{conv}(h(U)) \rightarrow \mathbf{R}^n$ defined by $\phi(y) = By + b$ for $y \in \text{conv}(h(U))$ is a left inverse of $h|_U$; that is, $x = \phi(h(x))$ for $x \in U$. Furthermore, for any convex combination $\sum_j \lambda_j h(d_j)$, $d_j \in U$, we have $\sum_j \lambda_j d_j = \phi(\sum_j \lambda_j h(d_j))$.

According to Lemma A, inversion of h is easy if h is piecewise linear with sufficiently large “redundancy number” ρ . Algorithm A exploits this, and produces state estimates with bounded error if Assumption A holds—that is, provided that the observations are redundant with sufficiently large redundancy number, and that the disturbances are small and bounded:

Theorem A.

If Assumption A holds, then there exists a $\mu \geq 0$ such that $\|x_k - \hat{x}_{k|k}\| \leq \mu \varepsilon_k$ for all k .

Algorithm A has a certain optimality property. That is, Algorithm A reduces to the maximum a posteriori probability (MAP) estimator under an ideal case.

Assumption B.

- (a) The output disturbance terms e_k are identically zero; that is, $\varepsilon_k = 0$ for all k .
- (b) The disturbances $x_0, w_0, v_0, w_1, v_1, \dots$, are all independent, and uniformly distributed on boxes $X_0, W_0, V_0, W_1, V_1, \dots$, respectively.
- (c) There are vectors $u_k \in \mathbf{R}^n$ and diagonal matrices $F_k \in \mathbf{R}^{m \times m}$, with $-I \leq F_k \leq I$, such that $f_k(x) = F_k x + u_k$ for $x \in X$.
- (d) The function h is one-to-one with a left inverse h^{-1} .
- (e) For all k , we have $V_k - V_k \subset W_k$.

In the ideal case where Assumption B holds, there exists a simple algorithm that generate MAP estimates:

Theorem B.

Suppose that Assumption B holds. Choose $\hat{x}_{0|0} \in X_0 \cap (h^{-1}(z_0) - V_0)$ and let

$$\hat{x}_{k+1|k} = f_k(\hat{x}_{k|k}),$$

$$\hat{x}_{k+1|k+1} = \arg \min \{ \|x - \hat{x}_{k+1|k}\| : x \in h^{-1}(z_{k+1}) - V_{k+1} \}$$

for $k = 0, 1, \dots$. Then we have $p_{k|k}(\hat{x}_{k|k} | z^k) \geq p_{k|k}(x | z^k)$ for all $x \in X$ and k . (For $x \in X$, $p_{k|k}(x | z^k)$ denotes the conditional probability density of $x_k = x$ given z^k .)

The optimization step in Theorem B is very similar to that in Step 4 of Algorithm A. In fact, Theorem B implies the following: if Assumptions A and B both hold, and if $\hat{f}_k = f_k$ for all k , then Algorithm A is the MAP estimator.

4.1.7 Angle of Incidence-Free Real-Time Wafer State Estimation

Like many optical *in situ* sensors, the 2CSR uses a fixed angle of incidence (AOI), and the RCWA model is obtained under the assumption that the exact value of the true AOI is known. However, it is found that small deviation of the assumed AOI from the true AOI can cause considerable error in real-time wafer state estimates, as well as least squares model fitting results. Thus, it is desirable to develop an AOI-free version of Algorithm A.

Let the true AOI be another state variable, denoted by θ_k at time k , whose evolution is given by

$$\theta_{k+1} = \theta_k, \quad k = 0, 1, \dots$$

Let Θ be the space of true angles of incidence. Then we have a function $\tilde{h} : X \times \Theta \rightarrow \mathbf{R}^m$ that represents the extended RCWA model such that

$$z_k = \tilde{h}(x_k + v_k, \theta_k) + e_k, \quad k = 0, 1, \dots$$

Choose a finite set T whose points form a uniform grid on Θ . Then by offline RCWA simulation, we obtain a sample of \tilde{h} given by $\tilde{\mathcal{H}}_{D \times T} = \{((d, \theta), \tilde{h}(d, \theta)) : d \in D \text{ and } \theta \in T\}$. Now, the AOI-free filtering problem is as follows: given $\{\mathcal{F}_k\}$ and $\tilde{\mathcal{H}}_{D \times T}$, get an estimate $(\hat{x}_{k|k}, \hat{\theta}_{k|k})$ of (x_k, θ_k) based on z^k for each k .

An analysis result in Section 6 indicates that, to have good state estimates, we may require $m \geq (n+1)3^{n+1}$, which is violated when $n = 3$ and $m = 92$. In fact, experiments show that direct use of Algorithm A for the AOI-free filtering problem does not yield satisfactory results, so we slightly modify Algorithm A: at time k , obtain an intermediate estimate $\tilde{x}_{k|k}$ of (x_k, θ_k) from Step 4 of Algorithm A; if $\tilde{x}_{k|k} = (d_1, \dots, d_n, d_{n+1})$, then set $\hat{x}_{k|k} = (d_1, \dots, d_n)$ and

$$\hat{\theta}_{k|k} = \hat{\theta}_{k|k-1} + \frac{d_{n+1} - \hat{\theta}_{k|k-1}}{1 + \lambda + \dots + \lambda^k} \text{ for some } \lambda \in [0, 1], \text{ where } \hat{\theta}_{k+1|k} = \hat{\theta}_{k|k}.$$

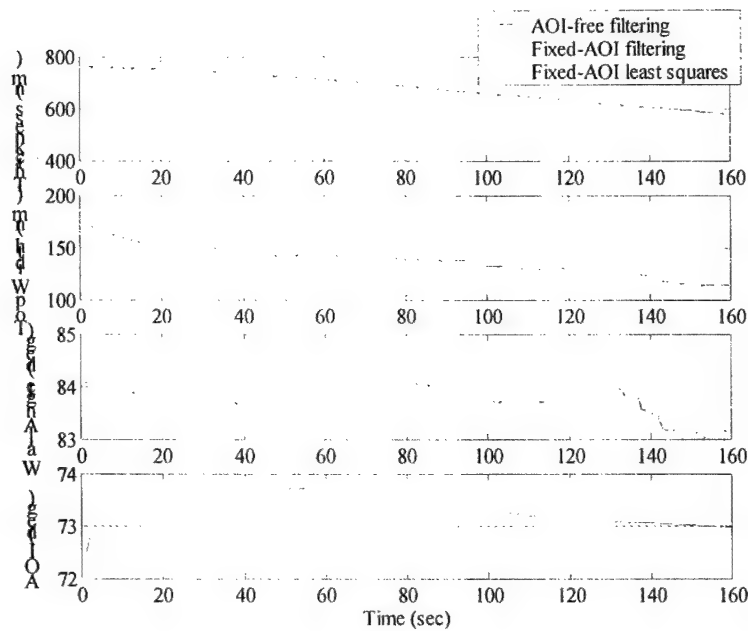


Figure 38

The above AOI-free algorithm has been shown to be capable of accurately estimating the wafer state in real time without knowing, or assuming, the true AOI value¹⁹. Figure 38 shows a typical result. The experimental data used in Fig. 2 are known to come from a true AOI $\approx 73^\circ$, so we re-used the data here. In the figure, the AOI estimates are shown to converge to (a small neighborhood of) the true AOI, and the resulting AOI-free wafer state estimates (solid lines) become virtually the same as the fixed-AOI estimates with assumed AOI = 73° (dashed lines) once the AOI estimates are sufficiently close to the true AOI.

4.1.8 Future Work

Next direction for extending our experimental result on the real-time state estimation for patterned wafers is to develop a more general model of patterned structures and analyze the corresponding optical sensor measurements. Analysis indicates that the proposed filtering algorithm can be applied to other systems with redundant observations and bounded disturbances—examples include power systems with redundant meter readings, and communication systems with redundant data.

1.1.1 References

- ¹⁰ B.S. Stutzman, H.-T. Huang, and F.L. Terry, Jr., "Two-channel spectroscopic reflectometry for in situ monitoring of blanket and patterned structures during reactive ion etching," *Journal of Vacuum Science & Technology B*, vol. 18, no. 6, pp. 2785-2793, 2000.
- ¹¹ M.G. Moharam and T.K. Gaylord, "Diffraction analysis of dielectric surface-relief gratings," *Journal of the Optical Society of America*, vol. 72, no. 10, pp. 1382-1392, 1982.
- ¹² T.L. Vincent, P.P. Khargonekar, and F.L. Terry, Jr., "An extended Kalman filtering-based method of processing reflectometry data for fast in situ etch rate measurements," *IEEE Transactions on Semiconductor Manufacturing*, vol. 10, no. 1, pp. 42-51, 1997.
- ¹³ H.-T. Huang, W. Kong, H. Kim, W. Sun, and F.L. Terry, Jr., "Normal incidence SE/RDS for critical dimension monitoring," in *The 195th Electrochemical Society Meeting*, 1999.
- ¹⁴ H.-T. Huang, B.S. Stutzman, and F.L. Terry, Jr., "Real time monitoring of grating structures using RCWA modeling and two-channel spectral reflectometry," in *APS Meeting*, 2000.
- ¹⁵ I. Kallioniemi, J. Saarinen, and E. Oja, "Characterization of diffraction gratings in a rigorous domain with optical scatterometry: Hierarchical neural-network model," *Applied Optics*, vol. 38, no. 28, pp. 5920-5930, 1999.
- ¹⁶ H.-T. Huang, J.-W. Lee, B.S. Stutzman, P. Klimecky, C. Garvin, P.P. Khargonekar, and F.L. Terry, Jr., "Real-time in situ monitoring of deep sub- μm topography evolution during reaction ion etching," in *AEC/APC Symposium XII Proceedings*, 2000.
- ¹⁷ H.-T. Huang, J.-W. Lee, P. Klimecky, P.P. Khargonekar, and F.L. Terry, Jr., "In situ monitoring of deep sub-micron topography evolution and endpoint during reactive ion etching," in *AEC/APC Symposium XIII Proceedings*, 2001.
- ¹⁸ J.-W. Lee and P.P. Khargonekar, "Simulation-based nonlinear filtering with redundant observations and bounded disturbances," in *Proceedings of the 40th IEEE Conference on Decision and Control*, 2001.
- ¹⁹ J.-W. Lee, H.-T. Huang, P.P. Khargonekar, and F.L. Terry, Jr., "Angle of incidence-free real-time state estimation for patterned wafers," submitted for publication in *AEC/APC Symposium XIV Proceedings*, 2002.

4.2 Design of Experiments

4.2.1 Process and Yield Improvement Through Spatial Modeling of Defect Clustering:

Methods for quality control and yield improvement in the IC fabrication industry have traditionally relied on overall summary measures such as lot or wafer yield. These measures are appropriate if the defective ICs are distributed randomly both within and across wafers in a lot. In practice, however, the defects often occur in clusters or display other systematic spatial patterns. These spatially clustered defects often have assignable causes due to specific process or equipment problems. Vijay Nair has collaborated with scientists and engineers from Bell Labs and Lucent Microelectronics to develop statistical methodology that exploits spatial information in wafer map data for process and yield improvement in IC fabrication.

These methods have been deployed extensively within Lucent Microelectronics and have led to considerable benefits in process and yield improvements. Presentations of the results have been given at various conferences including a workshop at the SEMATECH symposium in Austin, TX in May 1999.

4.2.1.1 Monitoring of Spatial Processes in Semiconductor Manufacturing:

This research developed novel statistical process control (SPC) methods to automatically detect the presence of severe spatial clustering of defects. A family of control charting procedures was developed and its properties studied under a Markov random field model of mild spatial clustering as well as under different patterns of large-scale clustering. Based on this, a specific method was proposed and its usefulness demonstrated through applications to real data.

4.2.1.2 Process Improvement Through the Analysis of Spatially Clustered Defects on Wafer Maps:

This research develops an overall strategy for yield improvement in integrated circuit fabrication by exploiting important spatial information in wafer map data. Both visualization tools and flexible methods of analysis are developed to analyze the high-dimensional and highly structured data. Algorithms for identifying spatial patterns at the wafer and lot level are developed. These are used to develop failure diagnostics and the spatial signatures are related to potential manufacturing problems in order to improve the manufacturing process.

4.2.1.3 Yield Modeling in IC Fabrication:

There has been tremendous interest in developing yield models as a function of device size and complexity so that reliable capacity and cost estimates can be obtained. Most of the research in the literature has focused on developing statistical distributions, such as the negative binomial, that would better fit the marginal yield data. Such models miss critical information available in the actual spatial distributions of defects. This research developed model-free methods for estimating some of the commonly used yield metrics that are used to track IC fabrication processes. These methods are shown to be superior to the time-honored windowing techniques that are used extensively.

4.2.1.4 Spatial Mixture Modeling and Cluster Detection:

This research develops a new methodology which models the wafer map data in IC fabrication processes as mixtures of spatially homogeneous Markov random fields. A Bayesian hierarchical model and Markov Chain Monte Carlo (MCMC) methods with Gibbs sampling are used to estimate the underlying model parameters. The ICM (iterative conditional mode) algorithm provides a quick way to "recover" the spatial clustering pattern. The techniques are illustrated on binary probe yield data and count data on particulate defects in IC fabrication. This work was part of Li-an Xu's Ph. D. thesis which was completed in May, 2000.

4.2.2 Optimal Design of Experiments for Modeling Processes with Feedback Variables:

To design a feedback control system, one has to first develop a model for the relationships among the input variables, potential feedback variables, and the output

variables and then select the appropriate variables for feedback control. This is typically done through statistically designed experiments where the input variables are systematically varied, and the experiment is run in an initial, open-loop mode without feedback control. Vijay Nair and Li-an Xu have studied the optimal design of experiments for modeling such a process. The paper considers a general statistical formulation of the problem and studies the properties of optimal designs in the linear case. Locally optimal designs under the D -optimality criteria are studied in detail, while results for A -optimality and Bayesian optimal designs are also developed. The results are used to characterize the potential loss in efficiency, under various situations, in using the classical designs for this problem.

This work was part of Li-an Xu's Ph. D. dissertation. This research is related to the Ph. D. thesis work of Oliver Patterson, done under the supervision of P. Khargonekar. Patterson's thesis examined methods for analyzing data from the experiment in order to select a suitable combination of variables for feedback control while this work studied methods for designing the experiment. The paper has been accepted for publication in the Journal of Statistical Planning and Inference. The research has been presented as invited papers at the Spring Research Conference on Statistics in Industry and Technology, Minneapolis in June, 1999 and at the Annual Statistics Society of Canada Meeting in Regina, June 1999.

4.2.3 PID Controllers and SPC for Auto correlated Data:

4.2.3.1 Efficiency and Robustness of PI Controllers:

Feedback control schemes have been in wide use in process industries for many years. They are also being used increasingly in the discrete-parts manufacturing industry recently. This paper studies the efficiency and robustness properties of discrete PI schemes under some commonly encountered situations. For process disturbance, we consider the stationary ARMA(1,1) model and the nonstationary ARIMA(1,1,1) model. Process dynamics is studied under a first-order dynamic model, including the special case of pure gain. The efficiency of PI schemes is compared with that of minimum mean squared error (MMSE) schemes under these models. The PI schemes are seen to be quite efficient over a broad range of the parameter space. Further, the PI schemes are much more robust than MMSE schemes to model misspecifications, especially the presence of first-order non-stationarity. The results here provide additional justification for the use of discrete PI schemes. This is joint work between V. Nair, F. Tsung (Hong Kong), and H. Wu (Iowa State).

4.2.3.2 PID-based Control Charts for Process Monitoring:

Using the connection between a PID-control scheme and the corresponding predictor, this research develops a class of control chart procedures for process monitoring, especially for use with auto-correlated processes. This PID-based scheme includes as special cases

several well-known and popular techniques, such as the EWMA and EWMAS (P-based) and Montgomery and Mastrangelo (I-based) charts. The performance of the procedures is studied under mean shifts and various auto-correlation structures. It is shown that performance within this class of procedures can be optimized by tuning the chart parameters through appropriately defined capability indices. Examples are given to illustrate the design and performance of the procedures. This is joint work with W. Jiang and F. Tsung of Hong Kong University of Science and Technology, H. Wu of Iowa State University, and K. L. Tsui of Georgia Tech.

5 Process and Materials Research

In this area, there were 3 major accomplishments achieved under this program:

1. Development of a novel ion-beam modification process for the deposition of Al films which are more resistant to grain-growth.
2. Development of improved plasma deposition processes for the manufacture of high performance AMLCDs.
3. The development of a new measurement technique for infrared measurement of thin film properties without substrate interference.

These results have been covered in detailed in prior annual reports in this program. During the final phase of this program, funding in these areas was curtailed and no significant new result were produced after the year 2000 annual report.

6 Faculty, Staff, and Students Supported

Faculty

J. Freudenberg
J. W. Grizzle
P. Kabamba
P. P. Khargonekar
D. Koditschek
M. Kushner (Illinois)
V. Nair
D. Srolivitz
F. L. Terry, Jr.
G. Was
C. F. J. Wu

Research Staff

D. Grimard
S. Rauf, (Illinois, Post-Doctoral Fellow)
W. Sun

Graduate Students

L. Dong
C. Galarza
C. Garvin
E. Hamby
H. Kim
W. Kong
T. Li
Z. Ma
O. Patterson
B. Stutzman
T. Vincent
L. Xu
Q. Zhao

7 Publications

Ph. D. Dissertations

B. S. Stutzman, "Correlation of Process with Topography Evolution During Reactive Ion Etching," July, 2000. Now with the Coast Guard Academy.

H. M. Park, " ", August, 2000. Now with Intel Corporation.

Lian Xu, "Statistical Issues in Semiconductor Manufacturing," May, 2000. Now with Bristol-Myers & Squibbs.

Journal Publications

1. S. Rauf and M. J. Kushner, "A Model for Non-Collisional Heating in Inductively Coupled Plasma Processing Sources", *J. Appl. Phys.* **81**, 5966 (1997)
2. S. Rauf and M. J. Kushner, "A Self Consistent Analytical Model for Non-Collisional Heating in Low Pressure Plasmas", *Plasma Sources Science and Technology* **6**, 518 (1997)
3. S. Rauf and M. J. Kushner, "Argon Metastable Densities in Radio Frequency Ar, Ar/O₂ and Ar/CF₄ Electrical Discharges:", *J. Appl. Phys.* **82**, 2805 (1997)
4. S. Rauf and M. J. Kushner, "The Effect of Radio Frequency Plasma Processing Reactor Circuitry on Plasma Characteristics", *J. Appl. Phys.* **83**, 5087 (1998)
5. S. Rauf and M. J. Kushner, "Virtual Plasma Equipment Model: A Tool for Investigating Feedback Control in Plasma Processing Equipment", *Trans. Semiconductor Manufacturing*. **11**, 486 (1998)
6. S. Rauf and M. J. Kushner, "A Diagnostic Technique for Measuring Plasma Parameters Near Surfaces in Radio Frequency Discharges", *Appl. Phys. Lett.* **73**, 2730 (1998)
7. S. Rauf and M. J. Kushner "Controller Design Issues in the Feedback Control of Radio Frequency Plasma Processing Reactors", *J. Vac. Sci. Technol. A*. **17**, 704 (1999)
8. S. Rauf and M. J. Kushner, "Nonlinear Dynamics of Radio Frequency Plasma Processing Reactors Powered by Multi-Frequency Sources", *Trans. Plasma Sci.* **27**, 1329 (1999)
9. R. L. Kinder and M. J. Kushner, "Consequences of Mode Structure on Plasma Properties in Electron Cyclotron Resonance Sources", *J. Vac. Sci. Technol. A* **17**, 2421 (1999)
10. E. Hamby, P. T. Kabamba, and P. P. Khargonekar, "A Probabilistic Approach to Run-to-Run Control, " *IEEE Transactions on Semiconductor Manufacturing*, vol. 11, pp. 654-669, 1998.
11. T. Vincent and P. P. Khargonekar, "A Nonlinear Estimation Problem Arising from Drifting Sensor Gains, " *IEEE Transactions on Automatic Control*, vol. 44, pp. 509-520, 1999.
12. L. Dong and D. J. Srolovitz, "Texture Development Mechanisms in Ion Beam Assisted Deposition, " *Journal of Applied Physics* **84** [9], 5261-5269 (1998).

13. T. Li, J. Kanicki, M. Fitzner, and W. L. Warren, "Investigation of Hydrogen Evolution and Dangling Bonds Creation Mechanism in Amorphous Silicon Nitride Thin Films," AMLCDs '95, p. 123 (1995).
14. T. Li, C. Y. Chen, C. T. Malone, and J. Kanicki, "High-Rate Deposited Amorphous Silicon Nitride for the Hydrogenated Amorphous Silicon Thin-Film Transistor Structures," Mat. Res. Soc. Symp. Proc., 424, 43 (1996).
15. T. Li, and J. Kanicki, "Longitudinal Vibrational Absorption Modes of Hydrogenated Amorphous Silicon Nitride Thin Films," Mat. Res. Soc. Symp. Proc., 507, 535 (1998).
16. Tong Li and Jerzy Kanicki, "Microstructure Characterization of Hydrogenated Amorphous Thin Films in A Fringe-Free Environment," *Journal of Applied Physics* 85, 388 (1999).
17. Tong Li, Jerzy Kanicki, and Carol Mohler, "Method of Collecting Pure Vibrational Absorption Spectra of Amorphous Thin Films," *Thin Solid Films* 349, 283 (1999).
18. Tong Li and Jerzy Kanicki, "Observation of Incident Dependent Phonon Absorption in Hydrogenated Amorphous Silicon Nitride Thin Films," *Applied Physics Letters* 73, 3866 (1998).
19. "Microstructure characterization of amorphous thin solid films in a fringe-free environment," T. Li and J. Kanicki, *J. Appl. Phys.*, 85, p.388-396, 1999.
20. Hansen, M., Nair, V, and Friedman, D., 1999 "Process Improvement Through the Analysis of Spatially Clustered Defects on Wafer Maps," Technical Report No. 333, Department of Statistics, University of Michigan (under revision).
21. Hyun-Mog Park, Dennis S. Grimard, Jessy W. Grizzle, and Fred Lewis Terry, Jr., "Etch profile control of high-aspect, deep submicron a-Si gate etch," *IEEE Transactions on Semiconductor Manufacturing*, pp 242-254 (2001).
22. Pete Klimecky, Craig Garvin, Cecilia G. Galarza, Brooke S. Stutzman, Pramod P. Khargonekar, and Fred L. Terry Jr., "Real-Time RIE Metrology Techniques to Enable *In situ* Response Surface Process Characterization," *J. Electrochem. Soc.*, 148, pp. 34-40 (2001).
23. Tong-Li, Jerzy Kanicki, Wei-Kong, Fred L. Terry, Jr, "Interference fringe-free transmission spectroscopy of amorphous thin films," *Journal-of-Applied-Physics*, 88, pp. 5764-71 (2000).
24. B. S. Stutzman, H.-T. Huang, and F. L. Terry, Jr., "Two-channel spectroscopic reflectometry for *in situ* monitoring of blanket and patterned structures during reactive ion etching," *J. Vac. Sci. Techn.*, B18, pp.2785-93 (2000).

Submitted for Journal Publication

1. M. J. Kushner and D. Zhang, "An Electron Impact Cross Section Set for CHF₃", to be published in *J. Appl. Phys.*
2. D. Zhang and M. J. Kushner, "Mechanisms for CF₂ Radical Generation and Loss on Surfaces in Fluorocarbon Plasmas", submitted to *J. Vac. Sci. Technol. A*.
3. R. Kinder and M. J. Kushner, "Wave Propagation and Power Deposition in Magnetically Enhanced Inductively Coupled and Helicon Plasma Sources", submitted to *J. Vac. Sci. Technol. A*.

13. S. Rauf and M. J. Kushner, "Feedback Control of Inductively Coupled Plasma Reactors", 44th National Symposium of the American Vacuum Society, San Jose, October 1997.
14. S. Rauf and M. J. Kushner, "Feedback Control of Polysilicon Etching: Controller Design Issues", International Conference on Plasma Science, Raleigh, NC, June 1998.
15. S. Rauf and M. J. Kushner, "Multi-Frequency Operation of RIE and ICP Sources", 45th Annual Symposium of the American Vacuum Society, Baltimore, MD, November 1998.
16. G. Font and M. J. Kushner, "Scaling of Hollow Cathode Magnetrons for Metal Deposition", 52nd Gaseous Electronics Conference, Norfolk, VA, October, 1999. (Bull. Am. Phys. Soc. 44, 74 (1999))
17. R.L. Kinder and M. J. Kushner, "Simulations of Low Field Helicon Discharges", 46th Annual Symposium of the American Vacuum Society, Seattle, WA, Oct. 1999.
18. D. Zhang and M. J. Kushner, "Investigation of Si and SiO₂ Etch Mechanisms Using an Integrated Surface Kinetics Model", 46th Annual Symposium of the American Vacuum Society, Seattle, WA, Oct. 1999.
19. J. Lu and M. J. Kushner, "Sputter-Wind Heating in Ionized Metal PVD", 46th Annual Symposium of the American Vacuum Society, Seattle, WA, Oct. 1999.
20. M. J. Kushner and S. Rauf, "Real Time Control of Plasma Tools During Recipe Changes and Transients", 46th Annual Symposium of the American Vacuum Society, Seattle, WA, Oct. 1999.
21. G. I. Font, K. F. Lai, Q. Lu and M. J. Kushner, "Simulations and Experimental Measurements of a Hollow Cathode Magnetron Ionized Metal Plasma Deposition System", 46th Annual Symposium of the American Vacuum Society, Seattle, WA, Oct. 1999.
22. D. Zhang and M. J. Kushner "Surface and Gas Phase Reactions for Fluorocarbon Plasma Etching of Si and SiO₂", 27th IEEE International Conference on Plasma Science, New Orleans, LA, June, 2000.
23. J. Lu and M. J. Kushner "An Integrated Plasma Equipment-Feature Scale Model for Ionized Metal Physical Vapor Deposition", 27th IEEE International Conference on Plasma Science, New Orleans, LA, June, 2000.
24. M. J. Kushner, "Plasma Modeling for Design of Equipment, Processes and Real-Time-Control Strategies", AFOSR Computational and Applied Mathematics Meeting, St. Louis, August, 1999. (Invited)
25. M. J. Kushner, "Strategies for Rapidly Developing Plasma Chemistry Model", 52nd Gaseous Electronics Conference, Norfolk, VA, October, 1999. (Bull. Am. Phys. Soc. 44, 63 (1999)) (Invited)
26. M. Kushner, "Introduction to the Session in Honor of Will Allis", 52nd Gaseous Electronics Conference, Norfolk, VA, October, 1999. (Bull. Am. Phys. Soc. 44, 41 (1999)) (Invited)
27. M. J. Kushner, "Plasma Equipment Modeling: Fundamentals and Applications", Applied Materials Engineering and Technology Conference, Whistler, BC, Canada, May 2000. (Invited)
28. M. J. Kushner, "Modeling of Collisional, Low Temperature Plasmas: Fundamentals and Applications" (Plenary), 27th IEEE International Conference on Plasma Science, New Orleans, LA, June, 2000. (Invited)

29. M. J. Kushner and J. Lu, "Plasma Equipment Modeling for Process Design", 17th International VLSI Multilevel Interconnection Conference, Santa Clara, CA, June 2000. (Invited)
30. "Two-Channel Spectroscopic Reflectometry: *In situ* Monitoring and Process Control Applications," Brooke S. Stutzman, Hsu-Ting Huang, Fred L. Terry, Jr., Pennwell Metrology 2000 Conference, San Jose, Ca., May 1-2, 2000.
31. "Real Time Monitoring of Grating Structures Using RCWA Modeling and Two-Channel Spectral Reflectometry," Hsu-Ting Huang, Brooke S. Stutzman, and Fred L. Terry, Jr., American Physical Society Meeting, Minneapolis, Mn., March, 2000.
32. Hsu-Ting Huang, Wei Kong, Brooke Stutzman, and Fred L. Terry, Jr., "Use of Spectroscopic Ellipsometry for Submicron Topography Measurements," SEMATECH AEC/APC Symposium, Vail, Co., September 13-16, 1999.
33. H. Kim, F. L. Terry, Jr. , "In-situ UV absorption CF₂ sensor for reactive ion etch process control," EOS/SPIE Conference on Microelectronic Manufacturing Technologies: Conference on Process and Equipment Control in Microelectronic Manufacturing, Edinburgh, Scotland, United Kingdom, May 18-21, 1999
34. Cecilia G. Galarza , Pete Klimecky, Pramod P. Khargonekar, Fred L. Terry, Jr., "In-Situ Design Of Experiments For A Reactive Ion Etching Process," MRS Spring Meeting, San Francisco, CA, April 7, 1999.
35. W. Kong, H. T. Huang, M. E. Lee, C. Galarza, W. Sun, and F. L. Terry, Jr., "Analysis of Time-Evolved Spectroscopic Ellipsometry Data from Patterned Structures for Etching Process Monitoring and Control," paper 19.2, SRC TECHCON, Las Vegas, Nevada, September 9-11, 1998. (won best paper award for Factory Control and Operations session)
36. M. E. Lee, C. Galarza, W. Kong, W. Sun, and F. L. Terry, Jr., "Analysis of Reflectometry and Ellipsometry Data from Patterned Structures," International Conference on Characterization and Metrology for ULSI Technology, Gaithersburg, MD, March 23-27, 1998, AIP Conference Proceedings 449, pp. 331-5 (1998).
37. B.S. Stutzman, H.-M. Park, P. Klimecky, C. Garvin, D. Grimard, D. Schweiger, and F.L. Terry, Jr, "In-Situ Real-Time Spectroscopic Ellipsometry Measurements on a LAM TCP 9400SE," Abs. 236, 195th Electrochemical Society Meeting, Seattle, Wa., May 2-6, 1999.
38. H.-T. Huang, W. Kong, H. Kim, W. Sun, and F. L. Terry, Jr., "Normal Incidence SE/RDS for Critical Dimension Monitoring," Abs. 244, 195th Electrochemical Society Meeting, Seattle, Wa., May 2-6, 1999.
39. Brooke S. Stutzman, Wei Kong, Hsu-ting Huang, Hunsuk Kim, Fred L. Terry Jr., "Measurement of Evolution of Grating Structures Using Off-Normal Spectral Reflectometry," abstract SC08.09, focus session on Industrial Applications of Optical Spectroscopy, American Physical Society Centennial Meeting, Atlanta, GA, March 20-26, 1999.
40. Brooke S. Stutzman, Fred L. Terry Jr., "Characterization of Film Thickness Using Off-Normal Spectral Reflectometry," abstract KW2.07, APS 51st Annual Gaseous Electronics Conference & 4th International Conference on Reactive Plasmas, Maui, Hawaii, October 19-22, 1998.

41. T. Vincent, C. Galarza, and P. P. Khargonekar, "Adaptive Estimation Using Multiple Models and Neural Networks," *Proc. 7th IFAC Symposium on Artificial Intelligence in Real-Time Control*, Grand Canyon, AZ, October 5-8, (Yo-Han Pao and S. R. LeClair, eds.) Pergamon, 1998.
42. O. D. Patterson and P. P. Khargonekar, "Methodology for real-time feedback variable selection for manufacturing process control: theoretical and simulation results," *SPIE Conference on Process, Equipment, and Materials Control in Integrated Circuit Manufacturing IV, Proceedings of SPIE*, Vol 3510, Sept 1998.
43. C. G. Galarza, P. Klimecky, P. P. Khargonekar, and F. L. Terry Jr., "*In situ* Design of Experiments for a Reactive Ion Etching Process," *Proceedings of 1999 Materials Research Society Spring Meeting 99*, San Fransisco, CA, USA; 1999; paper #U4.8, pp. 323. Source: Conference Record of the 1999 Materials research Society Spring Meeting, to be published September, 1999.
44. C. G. Galarza and P. P. Khargonekar, "A learning and estimation problem arising from *in situ* control and diagnostics of manufacturing processes," *Proc. 1999 American Control Conference*, pp. 854-859, San Diego, CA.
45. C. G. Galarza and P. P. Khargonekar, Fred L. Terry, "Real-time estimation of patterned wafer parameters using *in situ* spectroscopic ellipsometry," *Proc. IEEE Conference on Control Applications*, August 1999, Hawaii.
46. "Investigation of Hydrogen Evolution and Dangling Bonds Creation Mechanism in Amorphous Silicon Nitride Thin Films", T. Li, J. Kanicki, M. Fitzner, and W. L. Warren, presented at Second International Workshop on AMLCDs, September 25-26, 1995 in Bethlehem, PA.
47. "High-Rate Deposited Amorphous Silicon Nitride for the Hydrogenated Amorphous Silicon Thin-Film Transistor Structures", Tong Li, Chun-ying Chen, Charles T. Malone, and Jerzy Kanicki, presented at Materials Research Society Spring Meeting, April 8-12, 1996 in San Francisco, CA.
48. "Electrical Instability in High-Rate Deposited Hydrogenated Amorphous Silicon Thin Films", Tong Li, Chun-Ying Chen, Charles T. Malone, and Jerzy Kanicki, presented at Materials Research Society Fall Meeting, December 2-6, 1996 in Boston, MA.
49. "Longitudinal Vibrational Absorption Modes of Hydrogenated Amorphous Silicon Nitride Thin Films", T. Li, and J. Kanicki, presented at Materials Research Society Spring Meeting, April 13-17, 1998 in San Francisco, CA.

8 Industrial Interactions and Transfer

8.1.1.1 NIST-ATP Program

A NIST Advanced Technology Program for the Intelligent Control of the Semiconductor Patterning Process was started in part due to developments under this MURI Center. The goal of this program was to improve the control of the definition of the critical MOS transistor gate dimensions through sensor-based control of both the photolithography and reactive ion etching steps. The program was originally lead by National Semiconductor Corporation and the additional partners are KLA-Tencor, Lam Research, FSI International, the University of Michigan, and Stanford University. Major subcontractors include the University of California-Berkeley, the University of California-Irvine, and Cymer Laser Corporation. National Semiconductor left the program due to major restructuring of that company and KLA-Tencor assumed the lead partner position. The research leader of the program was Dr. Matt Hankison (KLA-Tencor). This program significantly aided in the effective transfer of some of our advanced control and sensing research to these industrial partners and some of their related suppliers.

8.1.1.2 Lucent Technologies - Bell Labs

Vijay Nair has collaborated with researchers at Bell Laboratories and process/product engineers at Lucent.

8.1.1.3 Plasma Modeling

The UI has a vigorous program of industrial interaction and technology transfer centered about our activities in plasma equipment modeling. Our research tasks on this MURI grant are able to leverage this existing infrastructure. The HPEM has been transferred to 12 industrial partners and 2 national laboratories, and updates of the HPEM based on MURI activities have been made available to all users.

Our industrial interactions relevant to the MURI tasks are as follows.

Company	Point of Contact	Leveraged Funding Source
AMD	Zoran Krivokapic zoran@grape.amd.com	SRC, NSF
Applied Materials	Dimitris Lymberopoulos Dimitris_Lymberopoulos@amat.com	Applied Materials, SRC

LAM Research	Tom Ni tom.ni@lamrc.com	LAM Research, SRC
Motorola	Michael Hartig mikeh@giedi.sps.mot.com	SRC, NSF
LSI Logic	Valery Sukhare vsukhare@lsil.com	SRC, NSF
Texas Instruments	Bill Dostalík dostalík@spdc.ti.com	SRC, NSF

9 Honors and Awards

Fellows

IEEE Fellows - J. W. Grizzle, P. P. Khargonekar, M. J. Kushner

American Statistical Association Fellows - V. N. Nair and C. F. J. Wu

American Physics Society Fellow - M. J. Kushner

Optical Society of America Fellow - M. J. Kushner

Institute of Mathematical Statistics Fellow - V. Nair and C. F. J. Wu

SEMI Outstanding Achievement Award - J. Moyne

American Society of Materials Fellows – D. Srolovitz and G. Was

NACE Fellow – G. Was

Best Paper Awards:

1. D. Srolovitz, American Institute of Chemical Engineering Annual Meeting, 1997.
2. T. L. Vincent, Best Paper Presentation in Session, American Control Conference, 1998.
3. Hsu-Ting Huang, Ji-Woong Lee, Brooke S. Stutzman, Pete Klimecky, Craig Garvin, Pramod P. Khargonekar, and Fred L. Terry, Jr., "Real Time In Situ Monitoring of Deep Sub- μ m Topography Evolution during Reaction Ion Etching," SEMATECH AEC/APC Symposium, Lake Tahoe, NV., September 25-28, 2000. (One of 4 best student paper awards at this conference)
4. P. Klimecky, C. Garvin, "Plasma Density & Resonant Cavity Modes vs. Chamber Condition in High Density RIE," SEMATECH AEC/APC Symposium, Lake Tahoe, NV., September 25-28, 2000. (best student paper award)
5. "In Situ Monitoring Of Deep Sub- μ m Topography Evolution And Endpoint Detection During Reactive Ion Etching," Hsu-Ting Huang, Ji-Woong Lee, Pete Klimecky, Pramod P. Khargonekar, and Fred L. Terry, Jr., SEMATECH AEC/APC Symposium XIII, October 6-11, 2001, Banff, Alberta, Canada (best student paper award honorable mention)
6. "Elimination of the RIE 1st Wafer Effect: Real-Time Control of Plasma Density," Pete I. Klimecky, Jessy W. Grizzle, and Fred L. Terry, Jr., SEMATECH Advanced Equipment Control/Advanced Process Control Symposium, Snow Bird, Utah, September, 2002. (best student paper award)